Organic Photodiode for Biometric Application System

ムハマド アフィク ビン ミスラン

https://hdl.handle.net/2324/6787637

出版情報：Kyushu University, 2022, 博士（工学）, 課程博士
バージョン：
権利関係：

Organic Photodiode for Biometric Application System

Muhamad Affiq Bin Misran

Kyushu University

2023

生体計測応用システムのための
有機光ダイオード

ムハマド　アフィク　ビン　ミスラン

九州大学

2023 年

Organic Photodiode for Biometric Application System

Muhamad Affiq Bin Misran

Thesis Submitted in Fulfillment for The Degree of
Doctor of Engineering

Department of Applied Science for Electronics and Materials
Interdisciplinary Graduate School of Engineering Sciences
Kyushu University
Japan

2023

ACKNOWLEDGEMENT

First and foremost, praise Allah S.W.T. the Almighty for giving me the blessing, strength, and endurance to complete this study.

I sincerely thank my supervisor, Professor Reiji Hattori, for his generous guidance, patience, and encouragement throughout the dissertation research.

I could not have finished this study without my beloved family, for their affection, love, encouragement, and continuous prayers have strengthened me in completing this study.

I want to extend my most profound appreciation to Green Asia Program for the scholarship and this golden opportunity to further my study here at Kyushu University.

I want to express my gratitude to all the staff and friends of the Green Asia program, Department of Applied Science for Electronics and Materials, Global Innovation Center, Interdisciplinary Graduate School of Engineering Sciences, and Kyushu University for their kind support and help on the technical and administrative aspects related to my study and living here in Japan.

I want to thank all the members of Hattori Laboratory (2016-2022) for their fruitful discussions and recommendations for completing my study. A special thanks to Mrs. Tomomi Minami and Mrs. Sayumi Waters for their continuous support, advice, and kindness in caring for me to ease my stay here in Japan. I also want to thank Dr. Chang-Hoon Shim and Dr. Anubha Bilgaiyan for their continuous support of my research here in this laboratory.

Last but not least, thank you to all of my friends in Malaysia and Japan for their motivational support and prays throughout my dissertation completion process.

ABSTRACT

With the advent of smartphone technology, numerous sensors and applications have been integrated into mobile devices. Plus, this technology can support and continuously modify people's lives, such as how they connect, shop, and conduct financial and banking transactions. Apart from mobile technology, one of the most important things to address is how people defend their rights, data, and private information in an insecure environment. As a result, security and complexity challenges arise. Over the last decade, many strategies have been created and tested to ensure user reliability when utilizing mobile devices and technologies. Thus, biometrics are used to identify individuals since they are unique. They represent something that exists in every human being.

Recently, smartphone makers are increasingly opting for a bezel-less display, eliminating the need for a fingerprint sensor on the home button. Thus, a thin-film fingerprint sensor within the display area would be an appealing option, despite the development of ultrasonic and thermal fingerprint sensors. Both have disadvantages: ultrasonic sensors are expensive for large-area display applications, and thermal sensor pictures have a short lifetime. Therefore, an optical fingerprint sensor based on solution-processed organic photodetectors (OPDs) could be used as an alternative. The OPDs based on organic semiconductors are a potential class of sensors that can provide these features. Their performance has increased rapidly in recent years, demonstrating their potential as a supplementary technology to inorganic devices. Most importantly, their solution processability allows for fabrication using industrial printing processes. The significant parameter space of printing, along with the morphological and energy

requirements of OPDs, creates a slew of obstacles to the transition from lab-scale to applicable production procedures.

However, there are still several issues related to the reliability of the optical fingerprint sensor, especially identity spoofing. On that account, several studies have been done recently to employ the Photoplethysmogram (PPG)-based authentication, which utilized the time-series bio-signals for biometrics. From this perspective, this dissertation provides a fundamental analysis of the optical simulation for human skin structure and fingertip structure at different distances and positions between the light source and detector for PPG sensor application. This analysis is done to understand the light propagation behavior in human tissues for better detection of PPG sensors. The simulation results show that the reflectance-based PPG principle has higher detection than the transmission-based principle. Plus, the reflectance-based is better in terms of applicability to any body parts.

Then, this study proposed the fingerprint-on-display (FOD) applications based on OPD devices for the biometric sensing application for the smartphone. This system uses the pinhole imaging technique, well-known for its immense images and straightforward structure. It combines optical sensors, which serve as image sensors, with a display for biometric fingerprint scanning. There are a few options for integrating this feature across the display area. Compared to inorganic photodiodes, OPDs benefit from large-area deposition capabilities, which can cover the entire display sensing area. The light distribution from a pinhole onto the sensor pixel was studied to observe the crosstalk and uniformity. Thus, recommending the critical parameters to improve the system in the future.

The evaluation focuses on the optical crosstalk between adjacent pixels for the organic image sensors using the interdigitated electrode structure. For applications requiring full-display sensing, the shorter exciton diffusion length of organic semiconductors in the OPD can support the high resolution of the organic image sensor. By adjusting the distance to determine the minimum pixel pitch for the organic image sensor, we could demonstrate the photocurrent diffusion from the exposed area to the buried electrodes. Unexpectedly, the observation shows that the photocurrent diffusion was more critical than the anticipated exciton diffusion length, even at 10 µm.

TABLE OF CONTENTS

LIST OF TABLES

LIST OF FIGURES

LIST OF ABBREVIATIONS

OPD	Organic Photodetector
FOD	Fingerprint on Display
IDE	Interdigitated Electrode
OPV	Organic Photovoltaic
OSC	Organic Semiconductor
PD	Photodetector
OLED	Organic Light Emitting Diode
LED	Light Emitting Diode
PPG	Photoplethysmography
Si-PD	Silicon Photodiode
BHJ	Bulk Heterojunction
HTL	Hole Transport Layer
HOMO	Highest Occupied Molecular Orbital
LUMO	Lowest Unoccupied Molecular Orbital
EQE	External Quantum Efficiency
CT	Charge Transfer
NEP	Noise Equivalent Power
UV	Ultraviolet
MC	Monte Carlo
DSLR	Digital Single Lens Reflex

CHAPTER I

INTRODUCTION TO BIOMETRIC AUTHENTICATION

1.1 RESEARCH BACKGROUND

Biometric recognition is a scientific field that identifies persons by measuring some aspects of their anatomy, physiology, or other behavioral characteristics.[1)] Biometric technologies provide a powerful authentication mechanism and are still being developed. Governments, forensics, and law enforcement agencies primarily support their spread to increase public security or a general sense of security. Biometric identification does not directly improve safety but functions as a disincentive to illicit activity.

These biometric qualities indicate the individual's physiological identity and cannot be transferred or misplaced. They are becoming increasingly crucial in-person identification solutions. Biometrics attributes are measurements taken from the living human body since the name biometrics is derived from the Greek words *bios* (life) and *metron* (measuring).[2)] Capturing a biometric characteristic with a biometric sensor (for example, a fingerprint scanner) generates a compact but expressive representation of the information (feature set). Then, those pieces of information are finally organized into one or more feature sets into an enrollment template, which will be saved into storage. Later, this biometric system can be used for verification or identification.

1.2 BIOMETRIC CHARACTERISTICS

The biometric characteristics can be divided into several parts, as shown in Figure 1.1. A brief explanation for each feature is provided as follows: -

a) **Fingerprint**: It is one of the biometric profiles with the most appealing characteristics. Fingers, and thus fingerprints, are found on every human being. They are exceedingly distinct and persistent; even if they vary slightly owing to skin scrapes and bruises, the fingerprint returns after the finger heals. Live-scan fingerprint scanners can capture high-quality fingerprint photographs by placing a finger on the sensor. Fingerprints have long been used in forensic sections for criminal investigations, and the technologies that support them are challenging to defeat. Fingerprint recognition is one of the most well-established biometric technologies and can be used for many applications.[3)]

b) **Face**: Face recognition is one of the most prevalent techniques people use to recognize other persons in their daily visual encounters. It makes it the most acceptable biometrics quality for the security verification process. The acquisition is simple and painless. However, the algorithms are very challenging to develop as they are invariant to age, expression, stance, and environment differences.[4)]

c) **Hand/palm**: Some aspects of the human hand are mainly similar, while others are unique to a person. The subject’s cooperation is required to acquire frontal and side-view photos of the palm. It is also possible to recognize the vein structure of the hand or finger using proper instruments (near-infrared imaging).[5)]

d) **Iris**: Iris recognition is another method to identify a person by examining their iris pattern. Here, a non-contact imaging procedure is usually used to obtain the image. However, this recognition method should not be confused with retina scanning, another ocular-based technology. John G. Daugman is the person who pioneered the development of this technology based on iris recognition algorithms.[6)] These algorithms are required for image collection and one-to-many matching. Iris identification is exceptionally accurate at high-resolution images and rarely hampered by glasses or contact lenses.

e) **Voice**: Voice access is not intrusive. Like a biometric attribute, it is unlikely to be sufficiently unique to allow a subject to be identified from an extensive database of identities. The voice signal is affected by elements such as a person’s health, stress, and emotional state, as well as the quality of the acquisition device.

f) **Signature**: A person’s signature is considered a trait of that person, yet it evolves through time and is impacted by physical and emotional factors. For a long time, signatures have been accepted as a verification technique in government, legal, and commercial transactions.

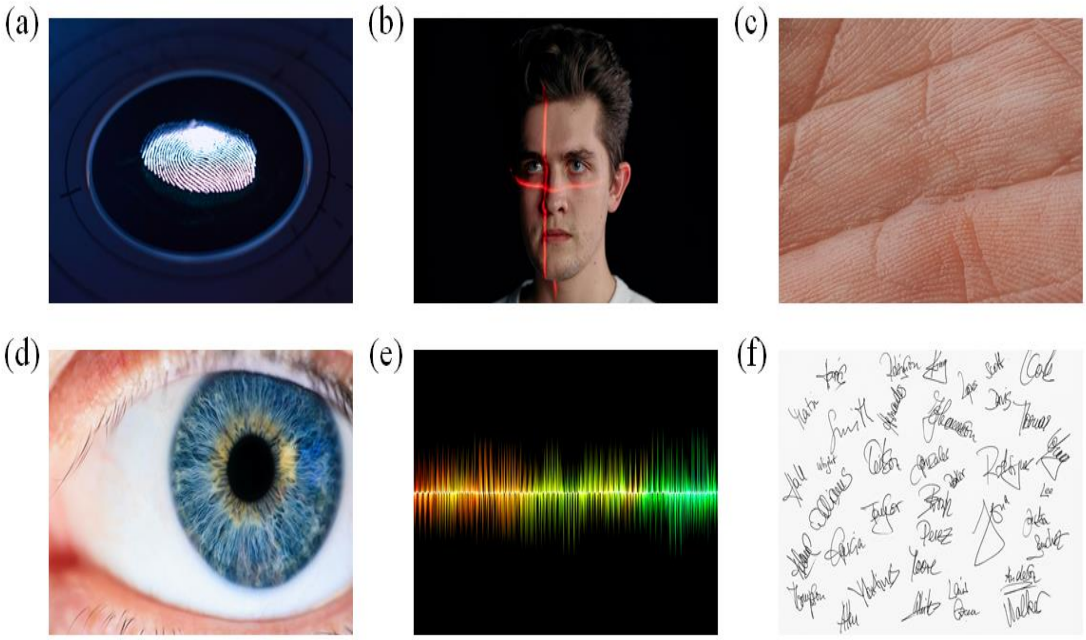

Figure 1.1 Biometric classification. (a) fingerprint, (b) face, (c) palm/hand, (d) iris, (e) voice, and (f) signature.

1.3 FINGERPRINT AUTHENTICATION

In recent years, full-screen smartphones with thin bezels and no physical buttons on the front display have become the norm. Fingerprint sensors, formerly housed under the home button, must now be placed on either the side or backside of the smartphones. Nevertheless, this fingerprint sensor is more convenient and intuitive if placed on the smartphone's front face. Fingerprint recognition has been developed in various ways for display technology, where capacitive, optical, and ultrasonic fingerprint sensors are the most common nowadays.[7)–13)] These methods are utilized in the current smartphones since they can be positioned underneath the display.

1.3.1 Optical Fingerprint Sensor

The oldest way of obtaining and comparing fingerprints is with optical fingerprint scanners. This method is based on the optical image capturing - essentially a photograph, as shown in Figure 1.2. Using algorithms, it then analyzes the image's lightest and darkest portions to discover distinctive surface patterns, such as ridges or marks. These sensors, like smartphone cameras, have a limited resolution. The finer details the sensor can discern about your finger, the higher the resolution and the higher the level of security.

On the other hand, these sensors capture images with far more contrast than a typical camera. When your finger is over the scanner, it's apparent that it's dark. As a result, scanners use LED arrays or your phone's display as a flash to illuminate the fingerprint surface during scanning.

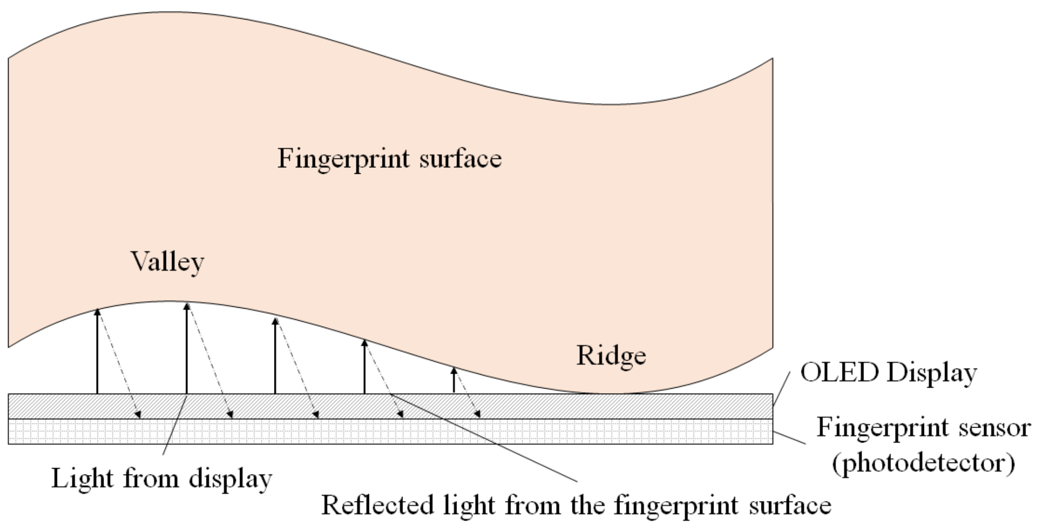

Figure 1.2 Optical fingerprint sensor

1.3.2 Capacitive Fingerprint Sensor

The capacitive scanner is another popular fingerprint scanner today. It can be found on most mid-range or high-end smartphones at the front, rear, or side. Due to their added security benefits, capacitive scanners have gained popularity. As the name implies, the capacitor is the fundamental component, as shown in Figure 1.3. Capacitive fingerprint scanners acquire data using arrays of tiny capacitor circuits rather than a typical fingerprint image. As the capacitors hold an electrical charge, we used them to track the specifics of a fingerprint by attaching them to conductive plates on the scanner's surface. The stored charge is somewhat altered when a finger's ridge touches the conductive plates. On the other hand, an air gap will leave the charge at the capacitor primarily unchanged.

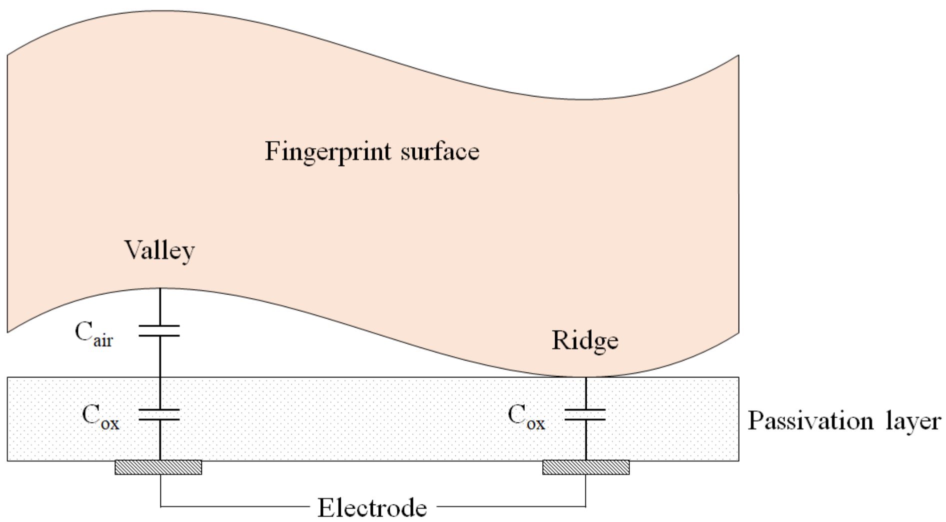

Figure 1.3 Capacitive fingerprint sensor

1.3.3 Ultrasonic Fingerprint Sensor

The ultrasonic sensor is the most recent fingerprint-scanning technology to join the smartphone market. Qualcomm was the first to reveal this technology within the Le Max Pro smartphone in 2016, where Qualcomm's Sense ID technology is the main element of the design. The 3D Sonic Sensor, Qualcomm's first-generation ultrasonic sensor, debuted in the Galaxy S10 phones in 2018. As time passes, Samsung's flagships, including the Galaxy S22, have since implemented Qualcomm's 3D ultrasonic in-display fingerprint sensor. The technology consists of an ultrasonic transmitter and a receiver to capture a fingerprint's features. An ultrasonic pulse is transmitted when a finger is put over the scanner. Everyone has the uniqueness of ridges, pores, and other characteristics on the fingerprint surface. Thus, the reflected pulse will differ depending on those characteristics, which are then sensed by the sensor.

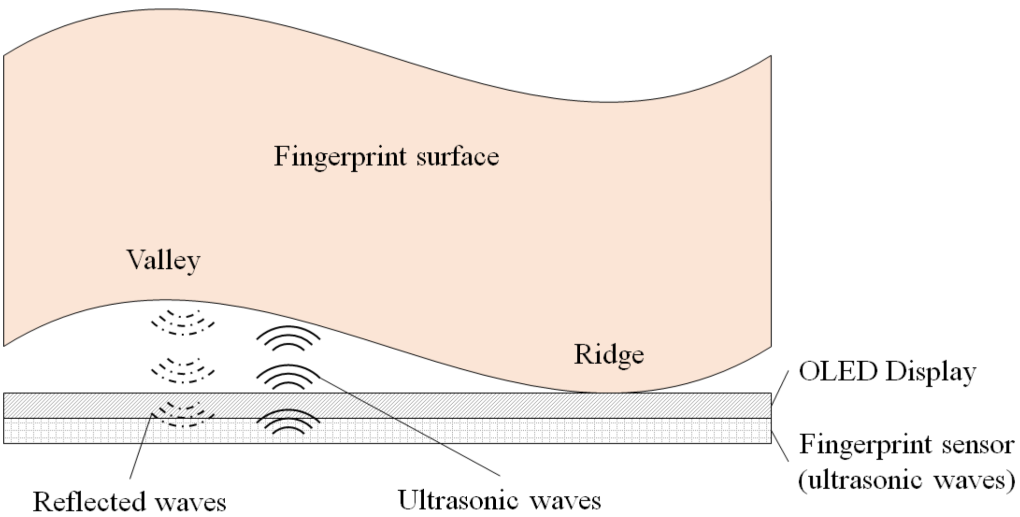

Figure 1.4 Ultrasonic fingerprint sensor

The trend in mobile phone design has been dominated by larger phones, up to the current maximum for user comfort while maximizing screen size, since the smartphone’s debut. The emergence of foldable displays will allow the trend mentioned above to continue. The latest models have an almost full-front side display. As the bezel and home button have been discarded in the recent model by the phone makers, the sensors must be integrated with the display to achieve sensing functionality beyond capacitive touch. Thus, it necessitates a high-resolution sensing solution in the display area for biometric recognition, which has traditionally been performed with a capacitive silicon-based sensor. Optical and ultrasonic sensing modalities have been the first demonstrated technologies integrated into a small display area. The technology for this purpose has been discussed previously, and the pros and cons are summarized in Table 1.1.

Table 1.1 Summary of optical, capacitive, and ultrasonic fingerprint authentication technology.

Method	Advantages	Disadvantages
Optical	- Can be embedded underneath the display. - Small footprint area.	- Insecure. - Recognizing issues on dry fingerprint surface. - Less consistency.
Capacitive	- Difficult to fool. - Lower cost.	- Week penetration. - Signal interference between touch panel and fingerprint identification signal.
Ultrasonic	- Highly accurate (3D mapping). - Hard to fool. - Work better even if the finger surface is wet/oily.	- Very expensive. - Complex processes.

1.4 PROBLEM STATEMENT

From the perspective of a full-front display for fingerprint authentication, implementing a thin-film fingerprint sensor within the display area would be an elegant option. Under this consideration, an optical fingerprint sensor based on solution-processed organic photodetectors (OPDs) would be an alternative. OPD-based sensors are ideal for this application because of their low process temperature feasibility for the solution process. These factors enable large-area photodetector arrays on thin, plastic substrates at a reasonable cost compared with other technologies for the full-display fingerprint sensor, as shown in Figure 1.5.

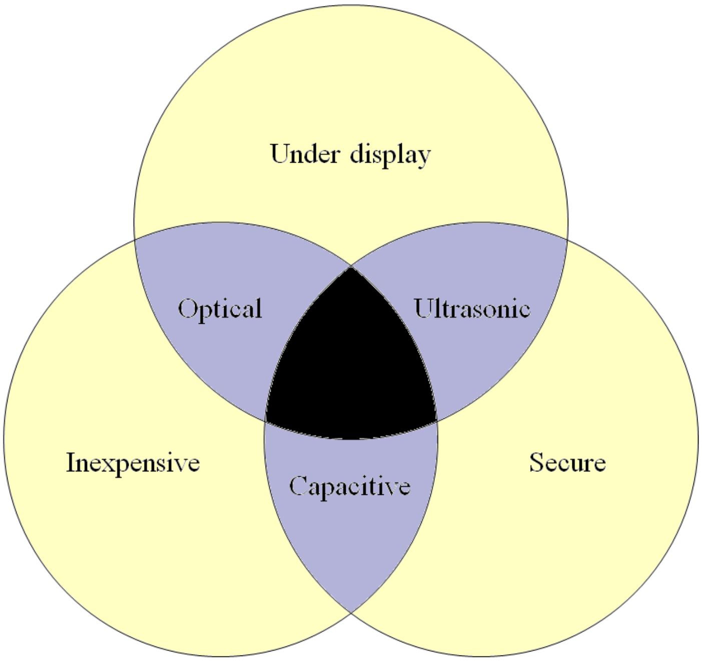

Figure 1.5 Simple classification of the advantages and disadvantages of the optical, capacitive, and ultrasonic fingerprint authentication.

As we proposed the use of optical sensing across the entire display area, new possibilities emerged:

a) The phone can be unlocked at any point on the smartphone display.

b) Specific apps can be secured by biometric access when pressing the icon.

c) The optical sensor array can be used for optical touch at a lower resolution and faster readout mode. In this case, it increases the potential to eliminate the need for an additional capacitive touch module.

d) The optical sensors can be used as ambient light sensors.

e) The display can act as the proximity sensor itself.

However, processing a large area of uniform thin-film OPD is quite challenging. The main issue with the optical system is the dry finger, which cannot create uniform and inconsistent contact with the surface of the sensor cover layer.

1.5 OBJECTIVE OF WORK

The objectives of the study here are:

a. To analyze the position of the photodetector from the light source for the PPG signal.

b. To observe the light propagation behavior in turbid media to enhance the PPG signal acquisition.

c. To analyze the pinhole imaging technique for implementing full-display fingerprint authentication.

d. To study the exciton diffusion length between the electrodes using the interdigitated electrodes (IDEs).

e. To estimate the crosstalk current between the pixels for the organic image sensor based on the exciton diffusion from the IDEs structure.

1.6 THESIS ORGANIZATION

This thesis includes six chapters that discuss the various theoretical and experimental findings. It is structured as follows:

CHAPTER I introduces the biometric authentication system technology currently available in the market. It also covers the issues related to biometric authentication applications for display technology and the aim of the work.

CHAPTER II briefly explains the fundamentals of OPD. It covers the working principle and architecture of the OPDs. The figures of merit for this device are also briefly described to understand the essential parameters. Additionally, the application of OPDs toward the large-area image sensor based on previous publications and contributions is provided in this chapter.

CHAPTER III introduces PPG signals based on principles and signal acquisition. The method used to observe the behavior of light propagation in the human skin and fingertip structure is described through the ray tracing technique. This simulation analyses the changes in the light propagation's behavior and the signals obtained from imitating the pulsating condition.

CHAPTER IV covers the pinhole imaging technique based on its principle and mechanism. It also introduces the implementation of this technique to the large area display sensing for the biometric authentication system. The analysis in this chapter covers a simple pinhole design for the display and observing the light distribution onto the sensors underneath the display passes through the pinhole structure.

CHAPTER V focuses on the organic image sensor device's crosstalk photocurrent analysis between neighboring pixels. The investigation will cover the exciton diffusion length in commonly used organic semiconductor materials for OPD devices. This analysis uses the IDE structure, especially for a simple spin-coating process of the device's fabrication.

CHAPTER VI summarizes the findings of all analyses throughout this thesis. Future works and recommendations are introduced in this chapter for development and enhancement.

CHAPTER II

ORGANIC PHOTODETECTOR

2.1 INTRODUCTION

Today's science and technology depend heavily on photodetection technology. Photodetectors are widely used in this technology. It converts the input photons into an electrical signal for the photodetection application. These devices are commercially available where it uses inorganic semiconductor-based materials such as silicon or compound from group III-V materials in the periodic table. They are commonly used due to their high charge-carrier mobility, low exciton binding energy, and excellent stability. However, the practical applications of commercial inorganic photodetectors are severely constrained due to several drawbacks, particularly regarding the requirement for large-area, flexible, and affordable devices. These drawbacks include complicated and expensive manufacturing processes and mechanical inflexibility.

Organic photodiodes (OPDs) are becoming more desirable for light-sensing applications. They have a fascinating combination of optoelectronics characteristics. Apart from that, the high photogeneration yield also is one of the factors which increased its feasibility. Those characteristics of affordable manufacturing costs, lightweight, and flexibility have attracted other researchers to focus on this device for various photo-sensing applications.[14)] Plus, Kudo *et al*. were the first to exhibit the OPD in 1981, showing the potential of organic semiconductors (OSCs) to control the spectral response in the form of OPD without color filters.[15] Additionally, thin active layers of only 100 nm are adequate to absorb up to 60% of the incident light due to the more significant absorption coefficients of organic materials (≈10^5 cm^{-1}) compared to silicon.[16)–21)]

Over silicon photodiodes (Si-PDs), OPDs offer additional benefits. First, they allow for the solution processing of large-area image sensors on a range of flexible substrates due to their compliance with the thermo-mechanical properties of plastic.[22] Secondly, OPD arrays are feasible to fabricate from the solution process at a lower temperature than amorphous silicon (usually less than 150°C).[23] Thus, utilizing industrially scalable coating processes, such as slot-die coating, opens the door to cheaper manufacturing costs. Furthermore, no diode patterning or alignment is necessary to integrate OPDs in large-area image sensors. The top-side absorbing OPD arrays with semi-transparent top electrodes provide more excellent resolution compared to imaging systems built on glass substrates, where light refraction and the resulting dispersion results in enhanced optical crosstalk between single pixels.[24]

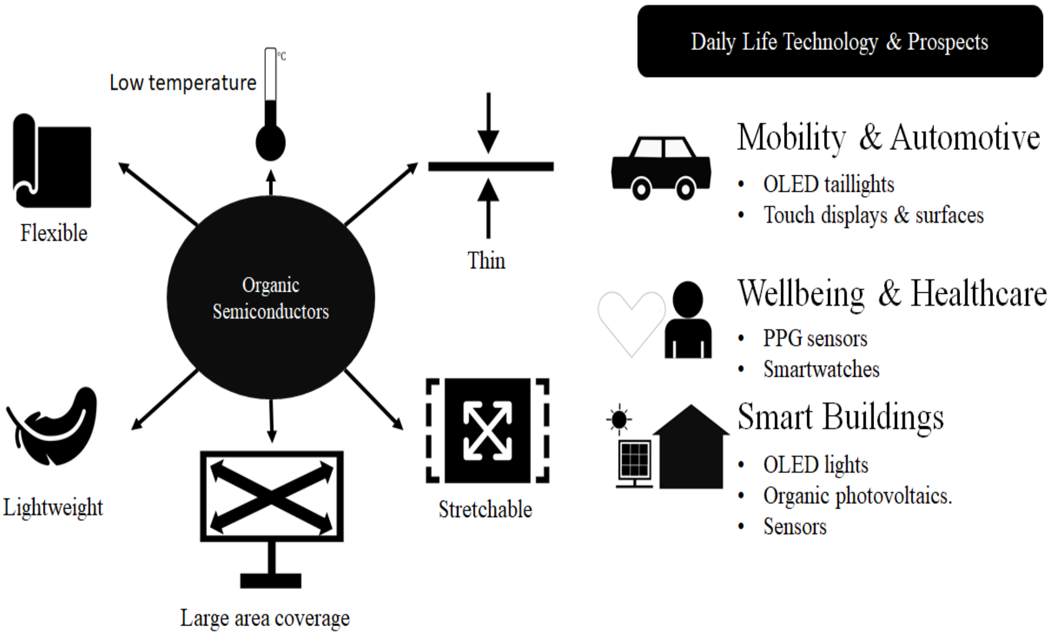

Figure 2.1 Benefits of OSCs with prospect applications.

OPDs now target a range of markets in the image sensor sector. Although compared to their inorganic equivalents, the longevity of OPDs for long-term applications is doubtful and has been a drawback. However, lifetimes of over 14000 hours under continuous operation have recently been shown for OPDs with cutting-edge characteristics.[25] A recent investigation demonstrates that an OPD-based image sensor is still functional after more than a year.[13] Furthermore, dangerous halogenated solvents like chloroform, chlorobenzene, and 1,2-dichlorobenzene are frequently used to deposit solution-processed active layers in OPDs.[24),26),27] Moreover, significant research has been put into developing photovoltaic devices processed using halogen-free solvents. Examples of halogen-free solvents are hydrocarbon solvents or water-based nanoparticle dispersions.[28)–30] Thus, using these solvents may pave the way for the eventual commercialization of more environmentally friendly OPDs.

2.2 OPD WORKING PRINCIPLE AND ARCHITECTURE

OSCs have a lower relative permittivity ($\varepsilon_r \approx 3 - 4$) than inorganic semiconductors. Instead of free carrier generation, the light absorption leads to photogeneration excitons with a relatively high binding energy between 0.35 and 0.5 eV.[31] In most cases, in the device fabrication of OPDs or even organic photovoltaic (OPVs), the bulk heterojunction (BHJ) structure is used to analyze its performance and functionality. This structure consists of finely intermixed percolating networks from the electron donor and acceptor phase.[32] Due to the large interface area between the electron donor and acceptor, these networks facilitate higher exciton dissociation. In contrast, the bi-continuous networks enable charge transport to the appropriate electrodes. A BHJ layer is sandwiched between two electrodes or at least one interlayer between the active layer and anode, such as a hole transport layer (HTL). Figure 2.2 depicts a typical OPD architecture.

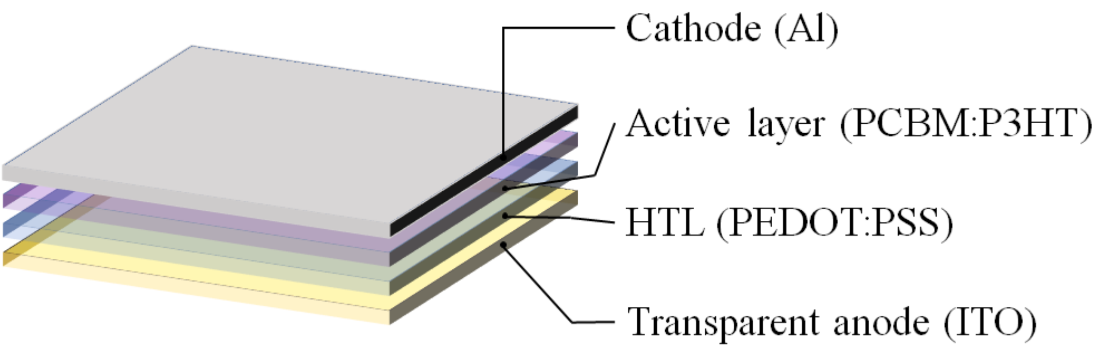

Figure 2.2 OPDs device architecture.

OPDs typically receive a negative bias voltage in contrast to OPV devices, which usually function under positive bias at the maximum power point. The OPD energetic band diagram with reverse-biased is shown in Figure 2.3. At the donor phase, photogenerated excitons split into free charge carriers, which drift to the appropriate electrodes due to the applied electric field. An effective electric field due to sufficient reverse-biased will extract all the photogenerated charges. Thus, generating the photocurrent, which is independent of the applied voltage.

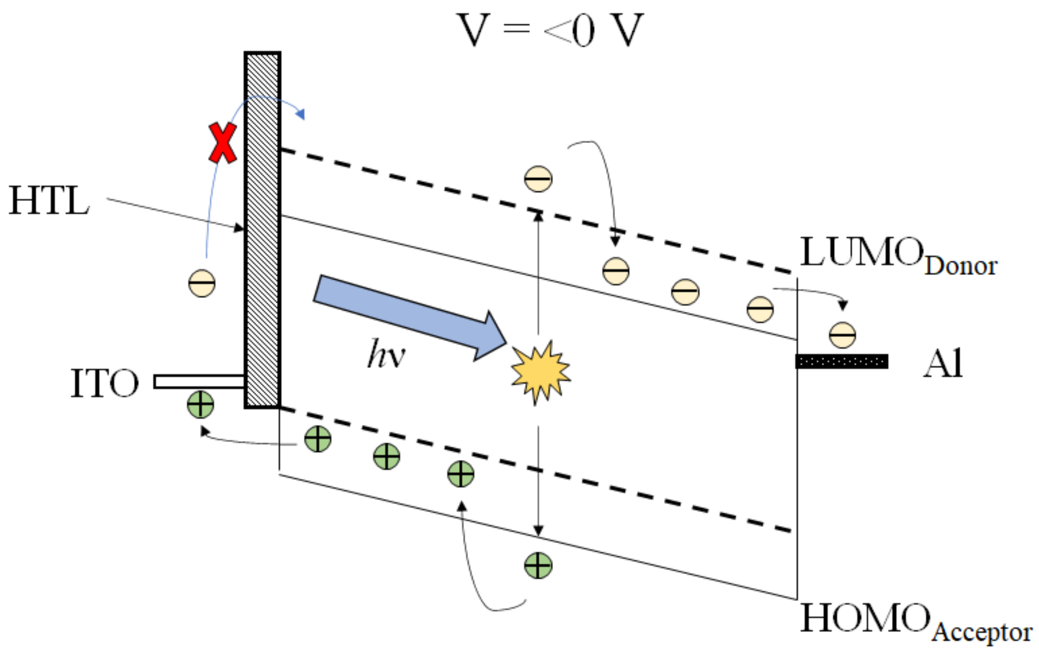

Figure 2.3 OPD mechanism upon illumination.

In terms of their internal workings and design, OPDs resemble OPVs. However, the objective of OPDs is to convert light signals into electrical signals, whereas that of

OPVs is to produce electrical energy from light energy. The demands for each device's performance differ since each type serves a unique purpose. The photoelectric conversion efficiency of OPVs is a crucial performance factor. The devices must balance the open-circuit voltage and fill factor while converting as much light energy as possible from the entire solar spectrum. It is then turned into an electric current to increase OPV's conversion efficiency.

Contrary to OPVs, which are made to absorb the entire sunlight spectrum, the spectral response range of OPDs needs to be adjusted for the application. Other OPD performance factors, such as their specific detectivity and response speed, are crucial in addition to their spectrum response. In addition, photodetector's performance can be improved by applying a reverse bias.

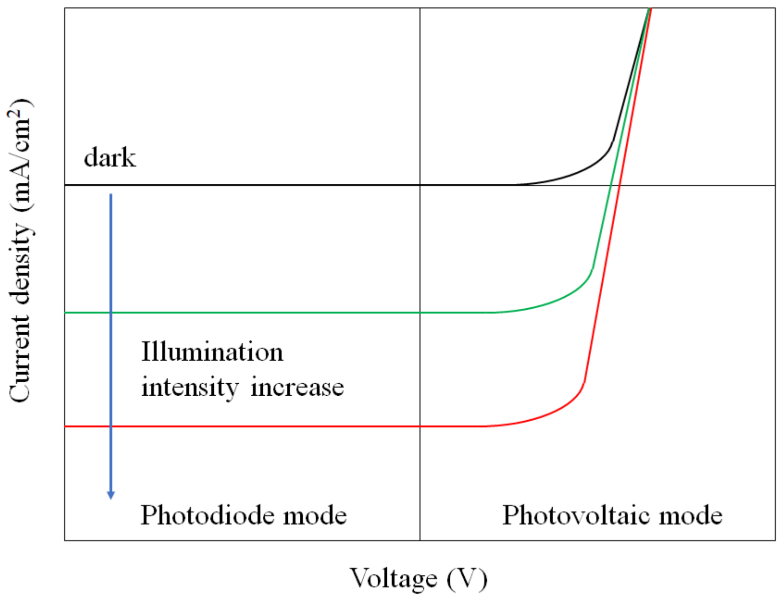

Figure 2.4 *I-V* curve of an OPD at different light intensities.

2.3 FIGURES OF MERIT

In this sub-chapter, we thoroughly characterize the crucial figures of merit to comprehend the reported OPD performances. Direct comparison of OPD performance can frequently lead to confusion because reported metrics are commonly measured using different experimental techniques and settings. From a critical viewpoint, we highlighted the range of testing procedures and the difficulties or limitations when comparing the reported data. We will also include the dependence on vital experimental variables, such as bias voltage, light intensity, and others.

2.3.1 *EQE* and Spectral Responsivity

The spectral responsivity, R (A/W), determined the produced current by the OPD per incoming photon at a specific energy. It can be determined using:

$$R = \frac{J_{ph}}{P_{in}}, \tag{2.1}$$

where J_{ph} (A/cm^2) is the photocurrent density, and P_{in} (W/cm^2) is the intensity of the incident light.[33)] The external quantum efficiency (*EQE*) is the ratio between the number of incoming photons and the number of photogenerated free electrons. It can be written as follows:

$$EQE = R\frac{h\nu}{q}, \tag{2.2}$$

where h is the Planck constant, v is the incident photon's frequency, and q is the elementary charge. High *EQE* (and thus *R*) is preferred to ensure effective photon flux detection. The *EQE* should ideally be spectrally invariant and as high as possible across the entire operational wavelength range for broadband OPDs. In the case of narrow-band OPDs, high *EQE* is crucial for the desired spectral window due to the requirement of color discrimination.[33)] In addition, the *EQE*'s spectrum absorption can be controlled by tuning the absorption characteristics of the donor and acceptor phase and the optical band gap. In a different method, charge collection narrowing is induced using a thick (about 2 μm) BHJ layer. In this case, only poorly absorbed photons will produce electrons close enough to the extraction layer to be collected.[34)] The micro-cavity effects can further boost the *EQE* in particular wavelength bands.[35),36)] Since the heterojunction OPD has the behavior of optical cavities, the multiple reflections between two semi-transparent metallic electrodes cause interference phenomena internally. Thus, increasing the absorption within the photoactive layer. It is then causing the spectral features of some wavelengths to be widened or narrowed. Recently, this phenomenon has been used by researchers to improve the *EQE* in the infrared region by enhancing the charge-transfer (CT) state absorption. These effects can be controlled by carefully adjusting the photoactive layer thickness and the characteristics of the optical spacer layers.[37)] Gathering numerous charge carriers per incoming photon or photomultiplication can also improve *EQE*. It is often accomplished in OPDs by trapped charge carriers bending energy bands, which enhances the charge injection under illumination conditions.[38)]

Finally, due to improved charge extraction efficiency, *EQE* (and consequently *R*) under reverse bias typically improves with higher applied voltage (i.e., electric field strength) but should eventually reach the saturation limit. Under reverse-biased, a trade-off between high EQE and low dark current density, J_d is implied that J_d will continue to rise as the electric field increases.

2.3.2 Speed of Response

After being created due to photon absorption, electrons and holes move toward the appropriate electrodes due to the applied electric field. The speed of response determines the OPD dynamic range and cut-off frequency. It measures the time needed to gather the photogenerated charge carriers at each contact.[39)] The impedance spectroscopy or time-of-flight photocurrent transients are commonly used to measure this response time.[40),41)] However, various methods may produce different experimental results at low charge carrier densities ($<10^{16}$ cm^{-3}) even though they probe through the same processes. It is because of surface recombination at the electrodes or an uneven charge distribution throughout the active layer.[42)] It is generally acknowledged that for polymer: fullerene BHJ OPDs, the transit time is constrained by the mobility of the slowest carrier, typically attributed to holes in the polymer phase.[43),44)] Transit durations for ordinary OPDs are in the order of µs for 100 – 300 nm thickness. Despite that, it is still shorter than the shortest interframe delay (33 ms) for imaging applications running at 30 frames per second (fps).[43)]

2.3.3 Noise Equivalent Power (*NEP*) and Specific Detectivity (D^*)

Noise equivalent power (*NEP*) is the lowest incident light power that the OPD can detect. The optical signal power resulting in a signal-to-noise ratio (*SNR*) of 1 is another definition of the *NEP*.[14] The *NEP* ($W/Hz^{1/2}$) can be written as follows using the description for the spectral responsivity provided by Equation (2.1):

$$NEP = \frac{i_{noise}}{R\sqrt{B}}, \tag{2.3}$$

where i_{noise} is the noise current, and *B* is the detection bandwidth.[33] The reciprocal of the *NEP* normalized to the square root of the device area, *A* is the specific detectivity *D**, measured in units of cm $Hz^{1/2}$ W^{-1} (i.e., Jones):

$$D^* = \frac{R\sqrt{AB}}{i_{noise}}. \tag{2.4}$$

Although a precise noise calculation is necessary to calculate *D**, experimental noise measurements are complicated and not frequently carried out. It is common to assume, for simplicity, that the shot noise, i_{shot} from the dark current, i_d makes up most of the noise, which results in:

$$D^{*} \cong \frac{R\sqrt{AB}}{i_{noise}} = \frac{R\sqrt{A}}{\sqrt{2qi_{d}}} = \frac{R}{\sqrt{2qJ_{d}}}. \tag{2.5}$$

J_d is assumed to be a constant value removed from the photoinduced signal in this notion. Equation (2.5) suggests that shot noise restricts D^* and dominates the dark current while ignoring 1/f noise and thermal noise.[45] This assumption may exaggerate the specific detectivity, as noted.[33),46] Therefore, it is possible to doubt Equation (2.5)'s general applicability. Additionally, there may be confusion when comparing reported D^* determined with Equation (2.5) due to two factors. The first factor is that J_d depends on the applied electric field. The second factor is R depends on the wavelength and applied light intensity according to Equation (2.1).

2.3.4 Dark Current Density (J_d)

Any current produced by a reverse-biased voltage in the absence of light is referred to as a dark current. The detrimental influence on several crucial metrics may measure the impact of high dark current density on OPD performance. First, increased J_d reduces sensitivity to low light intensities and causes a lower *SNR*. Additionally, lowering the minimum detectable photocurrent limits the image sensor's linear dynamic range (*LDR*) or the operational light intensity range.[33] Lastly, Equation (2.5) shows that the specific detectivity, D^* diminishes with increasing dark current densities. Reducing J_d is crucial for enhancing *SNR*, *LDR*, and D^* in OPDs. In contrast to R, J_d can range over multiple orders of magnitude depending on material qualities and device architecture.[25]

Lowering the dark current density in OPDs has received much attention lately. Modern OPDs show $10^{-6} – 10^{-7}$ mA cm^{-2} range values.[24)–26)] As J_d significantly depends on the applied bias, there is still no established standard procedure for measuring this parameter. Therefore, it can occasionally impede the direct comparisons of the reported results for the researchers.

2.4 OPD APPLICATION IN LARGE-AREA IMAGE SENSORS

OPDs are good choices for applications where the researchers desire conformity because of their flexibility. X-ray detectors, which are a well-established technology for digital radiography in the field of medical imaging, serve as an actual example. In conventional indirect conversion detectors, X-ray photons are typically converted into ultraviolet (UV) or optical photons by a scintillator layer. Then, the Si-PD array, installed on a rigid glass substrate, is used to detect it.[14)] The manufacturing procedure is greatly streamlined when Si-PDs are replaced with OPDs that have undergone solution processing, which lowers the fabrication cost. Compared to inorganic X-ray detectors based on rigid glass substrates, flexible X-ray image sensors are active under deformation and can adapt to complicated geometries, potentially enabling more accurate imaging of the human body.[47)] The first flexible photosensor array was demonstrated by Ng *et al.*, utilizing solution-processed OPDs on a flexible a-Si matrix backplane.[48)] Next-generation digital breast tomography systems were proposed by Zhao *et al.* in 2014. Their study used OPD-based X-ray imagers with amorphous indium gallium zinc oxide (a-IGZO) thin-film transistors (TFTs).[49)] Gelinck *et al.* demonstrated the X-ray imager fabricated using a solution-processed organic transistor array on a thin, flexible plastic substrate.[47)]

The OPD array also has been used to detect visible light reflected from the finger or hand, respectively, and for gesture recognition in biometric fingerprint and palmprint scanners prototypes.[50),51)] The difference in reflectance between the finger valleys and ridges is used to create fingerprint images. This technique is a low-cost replacement for bulky inorganic detectors. It is simple to incorporate into door handles or mobile phones. Compared to medical X-ray applications, fingerprint scanners need a better spatial resolution. A resolution of 200 pixels per inch (ppi) is typically necessary to unlock mobile phones. However, a higher resolution is required for high-quality fingerprint authentication, enabling more accurate sensing and, thus, a more considerable margin of safety. The detection of hand shadowing for gesture identification uses larger but poorer resolution arrays. Both applications demand reliable functioning under various lighting situations. Therefore, a linear photoresponse to the OPD is crucial. This can be done by using a second pulsed light source to modulate the OPD photoresponse and separating the temporal component from the time-invariant background contribution.

One of the prospects for OPD applications is the pulse oximeter sensor. It is a non-invasive device used to measure the oxygen saturation in the blood and monitor the heartbeat.[52),53)] Near-infrared (NIR) light is used, which minimally penetrates the skin before being partially absorbed or reflected. The organic pulse oximeters offer flexibility compared to conventional devices that often limit the sensing position to fingertips or ear lobes when used in reflective mode. Ideally, 850 nm light wavelength photoresponse can measure blood oxygenation levels.[53)] Usually, at least two different wavelengths of light are released one after the other. Thus, the light detection of each reflected hue can determine the degree of arterial hemoglobin oxygenation.

2.5 SUMMARY

OPDs have yet to be used in practical applications, despite OSCs showing significant benefits over inorganic semiconductors. One possible explanation is that the overall performance of OPDs is still inferior to that of inorganic photodetectors. The advantages of OSCs, such as flexibility, large area, and low cost, can bring many good things in the future, especially in light-sensing applications. Still, it has yet to be fully utilized. Most OPD research is currently being carried out by universities and research institutions, with only a limited amount of involvement from the companies. As a result, studies of OPDs tend to concentrate on fundamental and creative research. The device lifetime is another crucial constraint that restricts the practical use of OPDs. Most OSC materials are prone to degradation when exposed to water vapor, oxygen, and other contaminants. However, flexibility, transparency, and wearability will be crucial for producing more alluring electronic devices and maintaining product competitiveness to suit the expanding market requirements.[54)–56)] OPDs may be an excellent choice to realize all of the required features compared with traditional semiconductor materials.[47)]

CHAPTER III

PHOTOPLETHYSMOGRAPHY SENSOR SIMULATION

3.1 INTRODUCTION

The pulse oximeter is a non-invasive device that measures oxygen saturation in the blood as an initial procedure before further diagnosing a patient.[57] The data from the device is then utilized to assess various medical issues related to heart and lung function.[58] Pulse oximetry generally works on two principles, as shown in Figure 3.1. The principles are reflection and transmission and are readily available on the market.

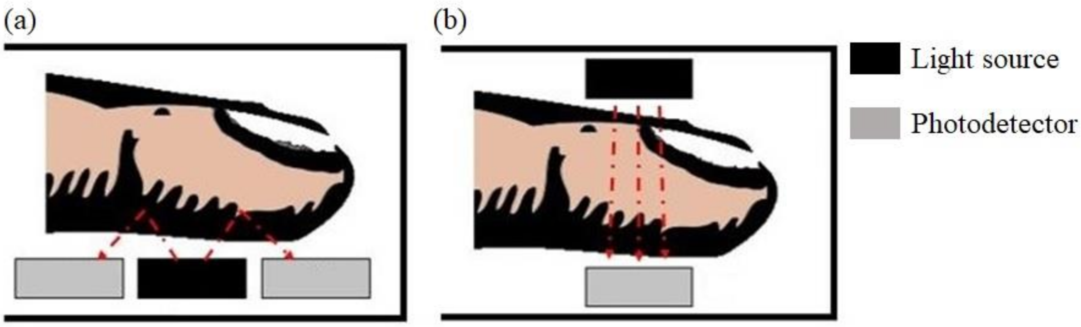

Figure 3.1 Principle of (a) reflectance-based and (b) transmission-based pulse oximeters.

Pulse oximeters are made up of two primary components. The light source and the photodetector are those components. The emitted light from the light source is absorbed, transmitted, scattered, and partially reflected in the skin, blood, bone, and other tissues under various situations. The photodetector is then utilized to generate an electrical signal by sensing the reflected light (reflection-based) or the varying intensities (transmission-based).[59] This electrical signal's AC pulsatile and quasi-static DC components contain two pieces of information.[60] As seen in Figure 3.2, these components combine to form the photoplethysmography (PPG) signal. The considerable DC component corresponds to light dispersion through tissues, venous blood, static arterial blood, and skin, as seen in Figure 3.2. On the other hand, the low AC signal is caused by variations in light absorption in arterial blood vessels during systole and diastole pulsation.[61] Since pulsation (blood flow) is governed by the brain, cardiac, and respiratory interactions, the signal can help provide some preliminary information about the user's health state.

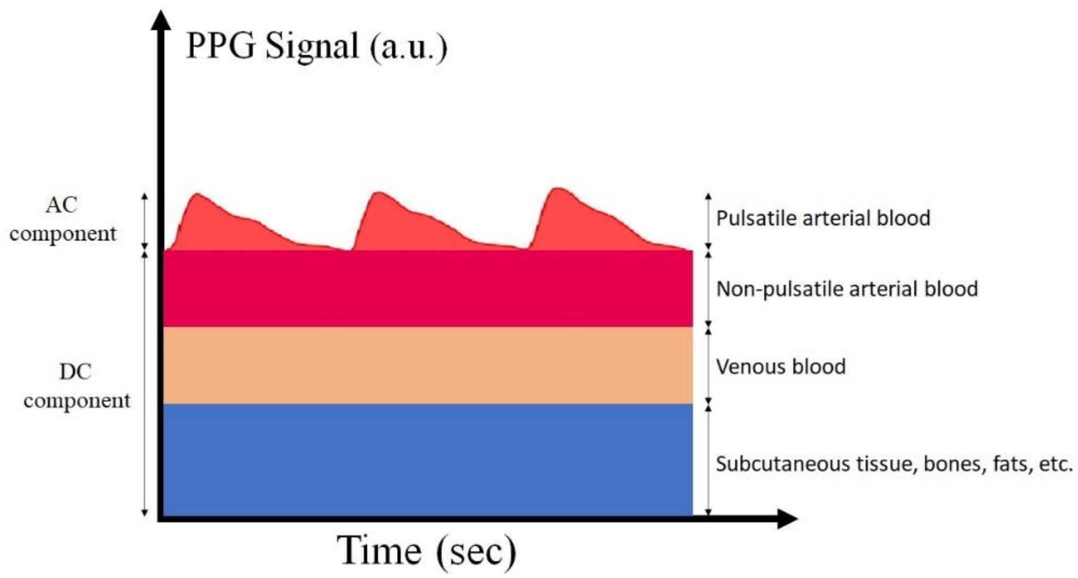

Figure 3.2 PPG signal components.

Several studies have been conducted in recent years to improve the pulse oximeter's performance, reliability, and feasibility, primarily as wearable daily health monitoring devices. Huang *et al.* demonstrated a multi-detector system ring-type pulse oximeter in 2014.[62)] They analyzed the effect of placing the light source and detector at different angles in the system and compared it with the multi-detectors approach for measuring arterial oxygen saturation (SpO_2). They also mentioned that employing a multi-detector system can improve PPG signal capture even further. They obtained more significant signals than the commercially available fingertip-type pulse oximeter. Elsamnah *et al.*, in 2019, built a reflectance-based pulse meter sensor with a circular organic light-emitting diode (OLED) surrounded by the OPD at two distinct distances.[63)] Shorter lengths have a more substantial *SNR*, according to their findings. As a result, the location of the light source and photodetector can significantly impact the PPG signals. However, information on the optical behavior of the finger structure or turbid media still needs to be included. Since the light scatters in the turbid media are very complex due to their systems and optical properties.

Optical human tissue simulation has been extensively investigated to understand turbid media's light characteristics and behaviors. This research is critical to improving the reliability of systems or applications that rely on a light source and photodetector as significant components. Hiraoka *et al.* used the Monte Carlo (MC) method to investigate the optical path length of the homogeneous tissue in the near-infrared (NIR) in 1993.[64)] In 2004, Reuss *et al.* employed this MC approach to examine arterial pulsation on a tissue model using reflectance pulse oximetry.[65)] Peris *et al.* built a custom MC technique platform in 2007, constructing the pulse oximetry mechanism using an opto-physiological model.[66)] In 2019, Chatterjee *et al.* used the MC approach to investigate the optical interactions in reflectance and transmittance finger PPG.[67] As a result, research into the interaction of light with human skin is required to provide helpful information for improving PPG devices.

We used the LightTools software and the MC ray tracing method to conduct this simulation. Based on the reflectance-based technique, a skin model was used to observe the internal ray tracing. A fingertip model was also used to monitor the ray tracing based on the reflectance and transmission principles. By varying the thickness of the highly oxygenated blood layer for the skin structure and the artery diameter for the fingertip structure, we attempted to mimic the pulsation state. Then, we estimated the optimum distance between the light source and detector for the pulse oximetry device.

3.2 MONTE CARLO (MC) SIMULATION

The optical simulation in this work was performed using the LightTools software with the MC method for the optical ray tracing. The model's geometry and structure are described in this section. Other details, such as the optical properties of the materials employed in the simulation, are also discussed.

3.2.1 Skin and Finger Structure

Figure 3.3 depicts the three primary layers of the skin tissue model employed in this simulation.[65),68)–72] The epidermis is made from dead cells and acts as a protective layer outside of the skin. The plexus superficial and plexus profundus layers make up the dermis, which is a cushion for the inner layer. This layer contains many blood capillaries, particularly in the plexus profundus, where the pulsatile state develops. The subcutaneous or hypodermis layer is mainly made up of fat and other tissues and is the bottom layer. Table 3.1 summarizes the creation of the skin model utilized in this simulation.[65),68)–72)]

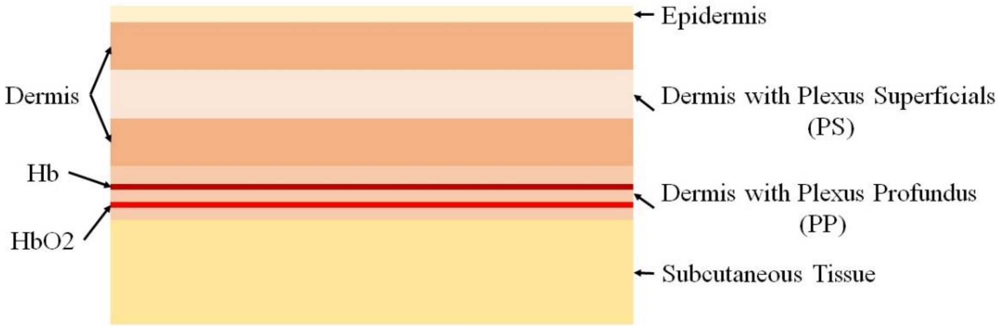

Figure 3.3 Skin tissue model.

Table 3.1 Human skin model thickness.

Layer	Sublayer	Thickness (mm)
Epidermis	-	0.2
Dermis	Dermis 1st layer	0.2
	Plexus Superficials	0.2
	Dermis 2nd layer	0.9
	Plexus Profundus	0.6
	Hb	0.06
	HbO_2	0.012 (initial)
		0.060 (pulsatile)
Subcutaneous Tissue	-	4.0

The basic fingertip structure was considered for simplicity, as shown in Figure 3.4, with the dimensions employed.[62),73)–76)] Muscles, bones, and tendons make up the structure of the fingertip, and the size of each varies from person to person. As a result, this model has no conventional size.

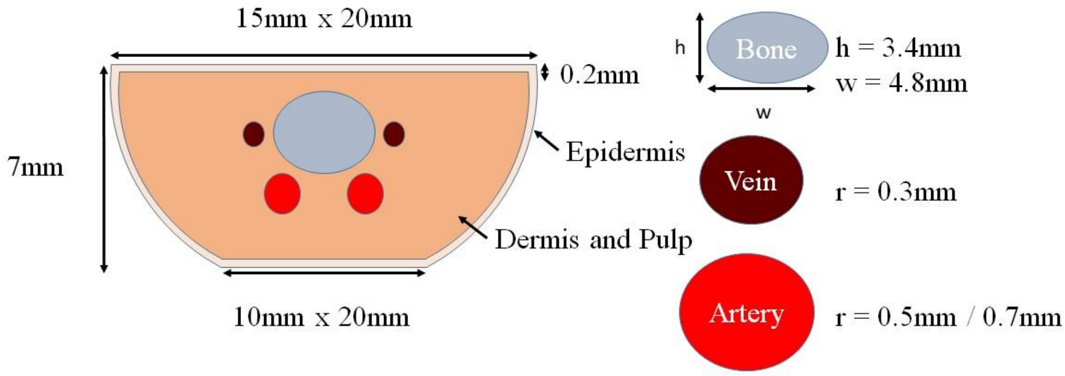

Figure 3.4 Fingertip structure model.

3.2.2 Optical Simulation by MC Method

Light is considered a bundle of photons conveyed across turbid media in the MC simulation. The paths of photons in the media are defined by statistically generated random numbers and described by several optical characteristics. The Henyey-Greenstein distribution is widely used in biomedical optics, and it is implemented in the LightTools software with the function:[77)]

$$p(\theta)=\frac{1}{4\pi}\cdot\frac{1-g^2}{\left[1+g^2-2g.\cos(\theta)^{\frac{3}{2}}\right]}, \tag{3.1}$$

where θ is the scattering angle, and g is the scattering anisotropy parameter. The value of g is represented by the cosine of the scattering angle as given by:[77)]

$$g \equiv \langle \cos\theta \rangle = \int_0^{\pi} p(\theta)\cos\theta . 2\pi \sin\theta d\theta . \tag{3.2}$$

A few critical elements for the optical human tissue simulation will determine the behavior of light scattering and distribution in human tissue. The refractive index (η), anisotropy parameter (g), absorption coefficient (μ_a), scattering coefficient (μ_s), and Mean Free Path (*MFP*) are the optical properties that are summarized in Tables 3.2 and 3.3.[62),65),78),79)]

Table 3.2 Optical properties of the human skin structure.

Material	***η***	***g***	μ_a (mm^{-1})	μ_s (mm^{-1})	***MFP*** (mm)
Epidermis	1.433	0.79	0.27	10.7	0.093458
Dermis with Plexus Superficials	1.396	0.82	0.27	19.2	0.052083
Dermis with Plexus Profundus	1.400	0.78	0.27	22.5	0.044444
HbO_2	1.363	0.98	0.20	77.5	0.012900
Hb	1.362	0.98	0.72	77.5	0.012800
Subcutaneous Tissue	1.370	0.75	0.003	5.0	0.20000

Table 3.3 Optical properties of the human fingertip structure.

Material	**η**	**g**	**μ_a (mm^{-1})**	**μ_s (mm^{-1})**	**MFP (mm)**
Epidermis	1.433	0.79	0.27	10.7	0.093458
Dermis and pulp	1.380	0.91	0.05	8.6	0.115600
Bone	1.400	0.92	0.05	33.1	0.030100
HbO_2	1.363	0.98	0.20	77.5	0.012900
Hb	1.362	0.98	0.72	77.5	0.012800

3.2.3 Simulation Process

The simulation was performed on the fingertip structure for both principles. However, the skin structure was not simulated for the reflection-based mechanism as it is not feasible in thicker areas of the human body, such as the arm and forehead. The arrangement of the light source and detector placement used in these simulations is shown in Figures 3.5 and 3.6.

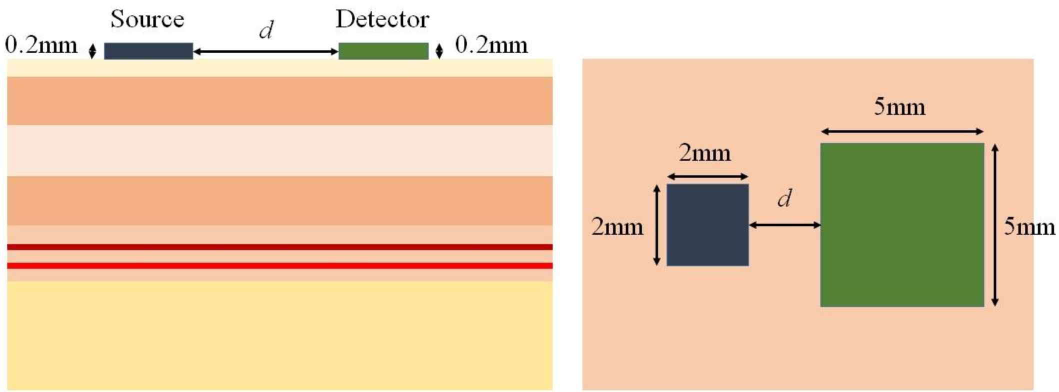

Figure 3.5 Reflectance-based for the skin structure.

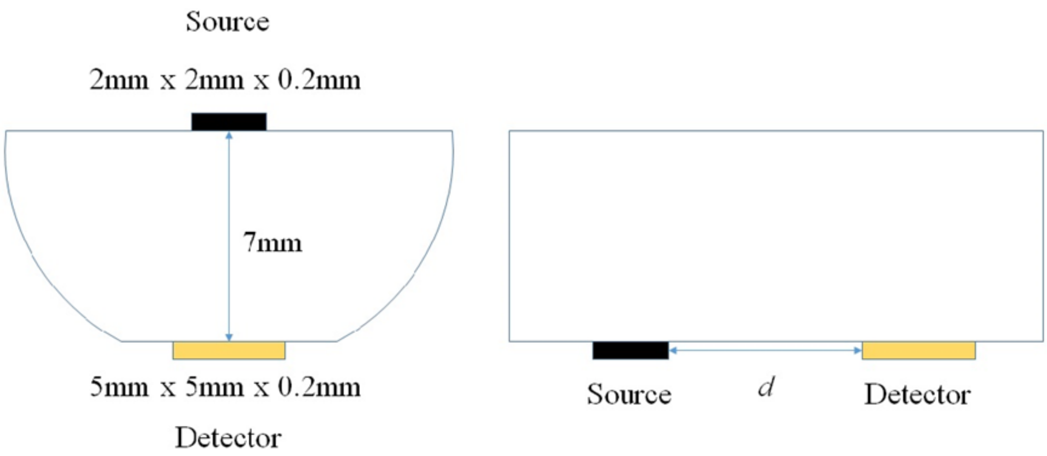

Figure 3.6 Transmission (left) and reflection (right) type of the simulation setup for the fingertip structure.

The light source in these simulations was a 633 nm (red light) wavelength at 1 mW radiometric power. It exhibits surface illuminance as well as Lambertian angular distribution features. At the same time, the detector employs surface detection to monitor and count the number of photons arriving at the detector's surface. The pulsatile condition was achieved by varying the thickness of the structure. The initial state is believed to be the diastolic mode, which reflects the DC component of the PPG signal. Based on Table 3.1 and Figure 3.4, the thickness or radius of HbO_2 in both structures was increased in systolic mode. The difference represents the AC component of the signal obtained from the simulation.

3.3 OPTICAL RAY TRACING

3.3.1 Ray Tracing

The ray tracing distribution under the scattering event in the skin model for the reflection-based concept is shown in Figure 3.7. The distance between the light source and the detector was 0 mm, and the light was only dispersed to the detector surface through the HbO_2 layer. In this simulation, we employed 10^5 rays for visualization only (as shown in Figure 3.7) and 10^8 for data collecting. Because the dermis layer has a more significant scattering coefficient than other components, most photons were scattered.

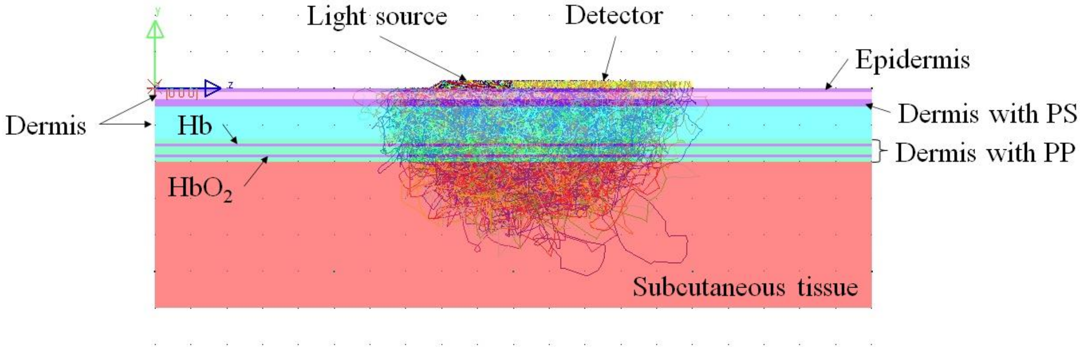

Figure 3.7 Filtered ray tracing distribution of the HbO_2 layer in the skin structure.

For the fingertip model, we set the distance between the source and detector to 7 mm for transmission and 0 mm for reflection-based principles. In the same way, the number of rays used was like the previous analysis. The 7 mm distance was chosen based on the assumption that a modest pressure was given to the fingertip. It occurs during the PPG measurement procedure, especially for the clip-type PPG device. According to Figure 3.8, the transmission-based theory reveals that the light source sends fewer rays to the detector surface. One of the explanations is the propagating light's comprehensive course of travel within the model. Another factor is the significant scattering effect of the bone structure, which hampered light propagation.

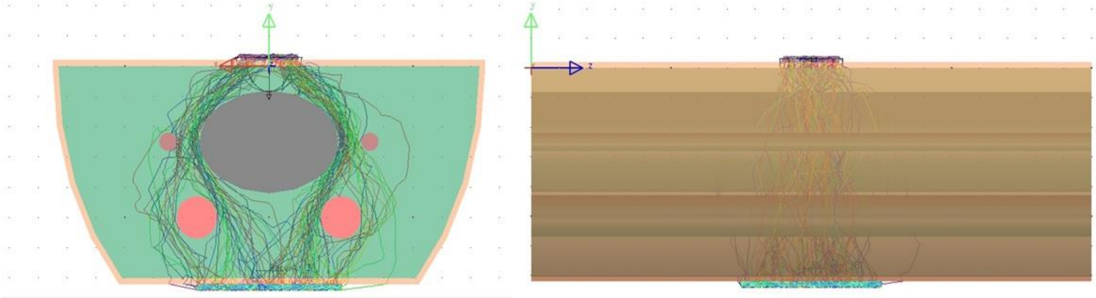

Figure 3.8 Ray tracing in the fingertip structure for the transmission-based with sectional view (left) and side view (right).

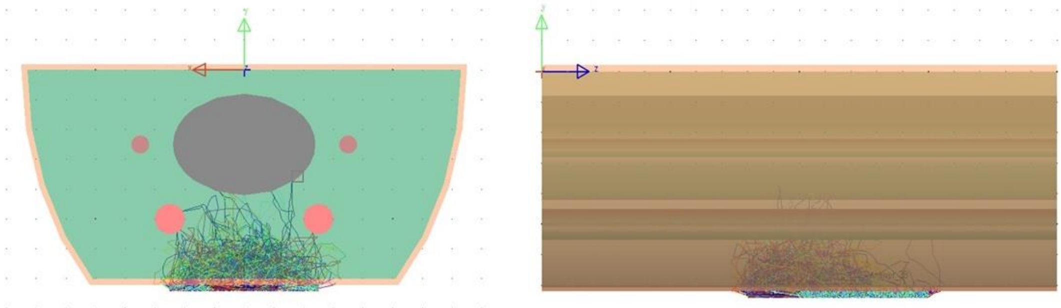

Figure 3.9 Ray tracing in the fingertip structure for the reflection-based with sectional view (left) and side view (right).

3.3.2 Pulsating Condition

Figure 3.10 depicts the skin model’s signal intensity (including DC and AC components) dependent on the number of photons detected on the detector’s surface at various distances from the light source. In both diastole and systole, the number of photons decreased as the distance between them increased.

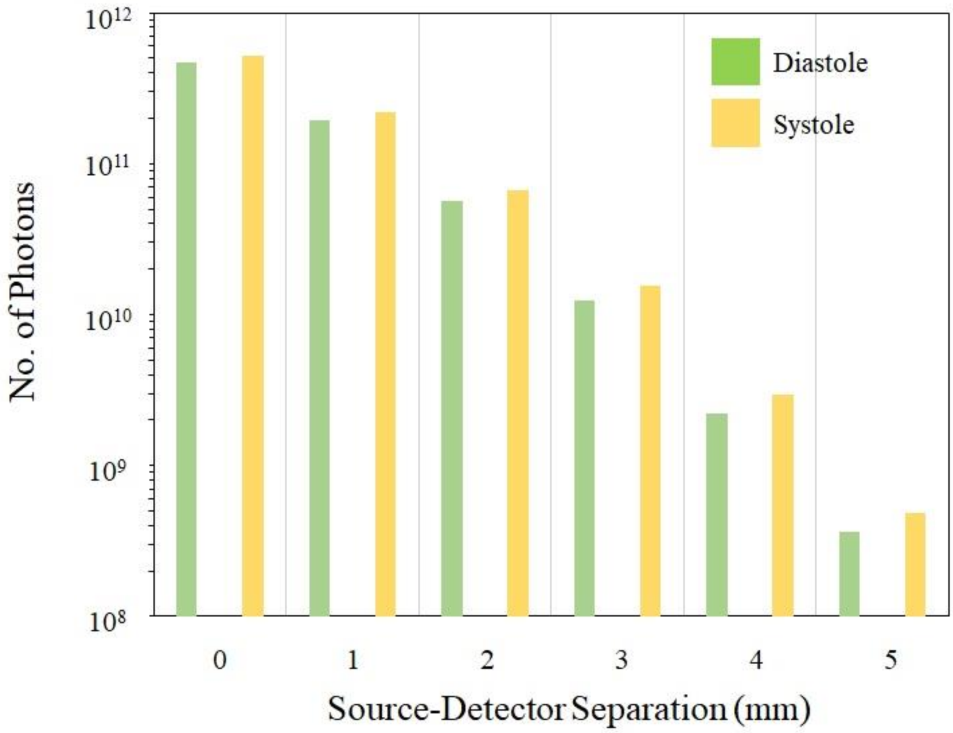

Figure 3.10 Number of photons detected at the sensor surface for the diastole and systole conditions for the skin structure.

We next converted the signals gained from the simulation into electrical signals and studied them further. The photocurrent was estimated based on the fabricated device, which was discussed in detail elsewhere.[61),63)] The current density was estimated by assuming the sensor has 40% of *EQE*. Figure 3.11 depicts the AC signals generated by the produced photocurrent at various distances from the source and detector. The predicted photocurrent density was reduced as we increased the distance. The estimated photocurrent was reduced for 0 mm to 2 mm between the source and detector. Still, it remained within a similar magnitude, around 10^{-10} A/mm^2. However, as we extended the spacing from 3 mm to 5 mm, we saw a considerable photocurrent reduction from 10^{-11} A/mm^2 to 10^{-12} A/mm^2. As we increased the distance between the detector and the illuminated area, we assumed it was due to the expanded traveling route of the rays from the interest area. Scattering events in turbid media also impact the reflected light that reaches the sensor.

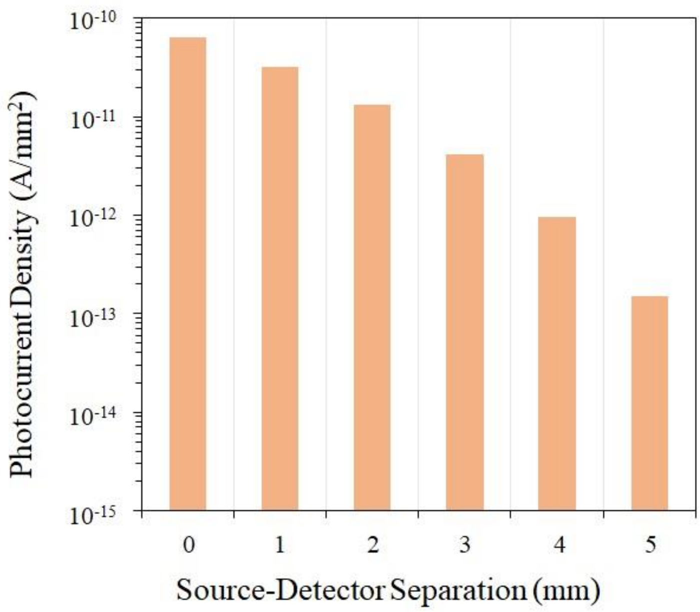

Figure 3.11 Estimated photocurrent density for AC component from the skin model at different source-detector separations.

On the fingertip structure, we also reproduced both principles. The goal was to see how the position of the source and detector affected the results. Figure 3.12 depicts the photocurrent density depending on reflection and transmission. As expected, even in the fingertip structure for the reflection-based, the closer distance between the source and detector has higher photocurrent density, similar to the simulated skin model results. However, the gap between 1 mm and 3 mm for both versions is slightly different. In the skin model, as shown in Figure 3.11, there was a linear decrease in photocurrent density. We suspected that the linearity is due to the homogeneous structure of our model. Despite that, the fingertip model showed a significantly higher photocurrent density at a 2 mm distance. These photocurrent densities from 1 mm, 2 mm, and 3 mm distances remained within a comparable order of magnitude around 10^{-12} A/mm^2, even though the rationale is still unknown. We noticed a considerable fall in photocurrent density at 10^{-14} A/mm^2 as we extended the distance to 4 mm and 5 mm.

At 4 mm and 5 mm distances, the photocurrent density of the transmission-based system was two orders higher than that of the reflection-based system, which shows around 10^{-12} A/mm^2. However, it is smaller than the values for 0 mm to 3 mm distances. The distance between the source and the detector significantly influences the sensing process. One of the critical explanations for the reduced photocurrent density measured is the bone structure between them. The opacity of the bone is higher than other components in the model. As a result, less light will be able to pass through the fingertip model and reach the sensor surface.

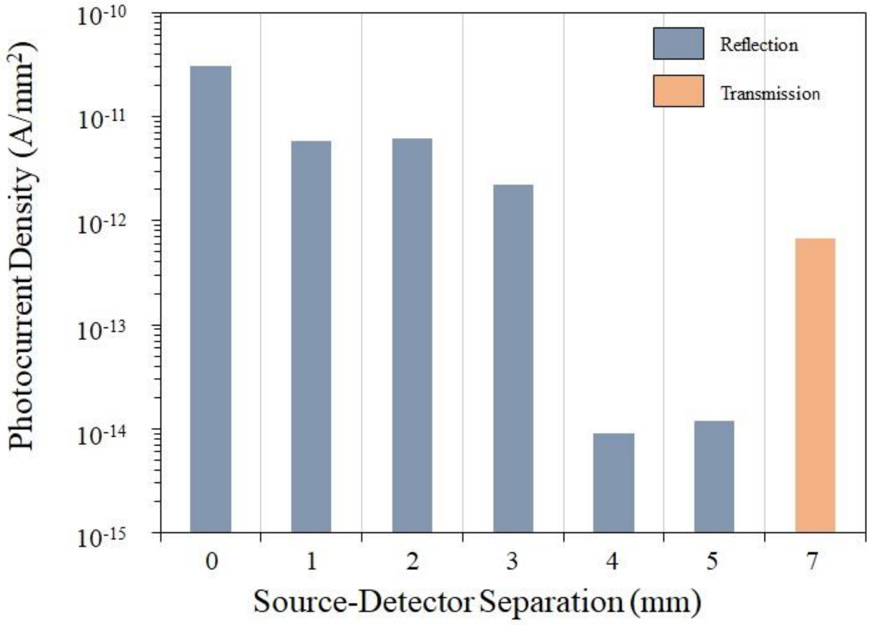

Figure 3.12 Estimated photocurrent density for AC component from the fingertip model at different source-detector separations for reflection and transmission-based.

3.4 SUMMARY

In summary, we simulated the PPG sensor device principle based on the optical interactions in the turbid media. We used the ray tracing MC simulation and investigated the impact of the distance between the light source and detector, especially for the reflectance-based approach. Based on the simulation results, the ideal separation should be less than 3 mm. Thus, we can improve the PPG signal acquisition. We also observed that positioning the light source and detector has a significant impact. It is due to the opacity of the bone structure, which reduces the transmission of light in the case of transmission-based PPG devices. In the prospect of the biometric authentication application, the sensor resolution is higher for better security. Thus, most of the pixel's pitch for the image sensor is less than 1 mm. Therefore, integrating a biometric authentication system with PPG signals is feasible where PPG signal acquisition is expected to be good enough.

CHAPTER IV

PINHOLE IMAGING ANALYSIS

4.1 INTRODUCTION

Researchers have recently demonstrated and incorporated optical and ultrasonic sensors into fingerprint-on-display (FOD) technology.[50),80)–82)] In the case of an ultrasonic sensor, the detection region is minimal. It is due to the size and positioning of the module underneath the display. On the other hand, optical sensing technology can fully exploit new possibilities, such as full-display sensing. It is feasible since most researchers have focused on the OPD for image-sensing applications. Thus, moving toward the biometric authentication system. Therefore, OPD can be one of the most promising candidates for the full-display biometric authentication system.[13),50),51),83),84)] Compared to inorganic PD, OPDs have various advantages, such as solution processability at the low-temperature process. It allows for large-area photodetector arrays on a thin plastic substrate and is very cost-effective.

The majority of FOD optical techniques on the market involve lenses and collimators. However, these lenses and collimators will increase the thickness of the display panel and integrating them with the display panel is a complex operation. In light of this, some panel manufacturers attempt to offer an alternate solution based on the pinhole matrix imaging approach.[85),86)] Pinhole imaging is well-known for its immense pictures and straightforward structure. Despite this, there is still a need for more knowledge about this technique for applying FOD. The pinhole's diameter and the distance between the pinhole and the object are critical parameters for the imaging system. As a result, we examined the light distribution from the pinholes to the sensor layer in this work using a two-dimensional aligned pinhole analysis. The image quality produced by this system was then evaluated using an image processing technique based on light distribution estimation.

4.1.1 Pinhole Camera Principle

In conventional optics, the pinhole imaging principle is used to realize lensless imaging. The idea of rectilinear light motion, which states that light moves in straight lines, is the foundation of pinhole cameras. Thus, it creates an inverted image due to the light's straight-line travel, as shown in Figure 4.1. A picture is imprinted on photographic paper or film at the camera's rear when the shutter is opened, allowing light to pass through. Then, we can create a good quality image under the proper exposure time with appropriate alignment between pinhole size and film size for the exposure. This picture quality can compete with the digital single-lens reflex (DSLR) camera.

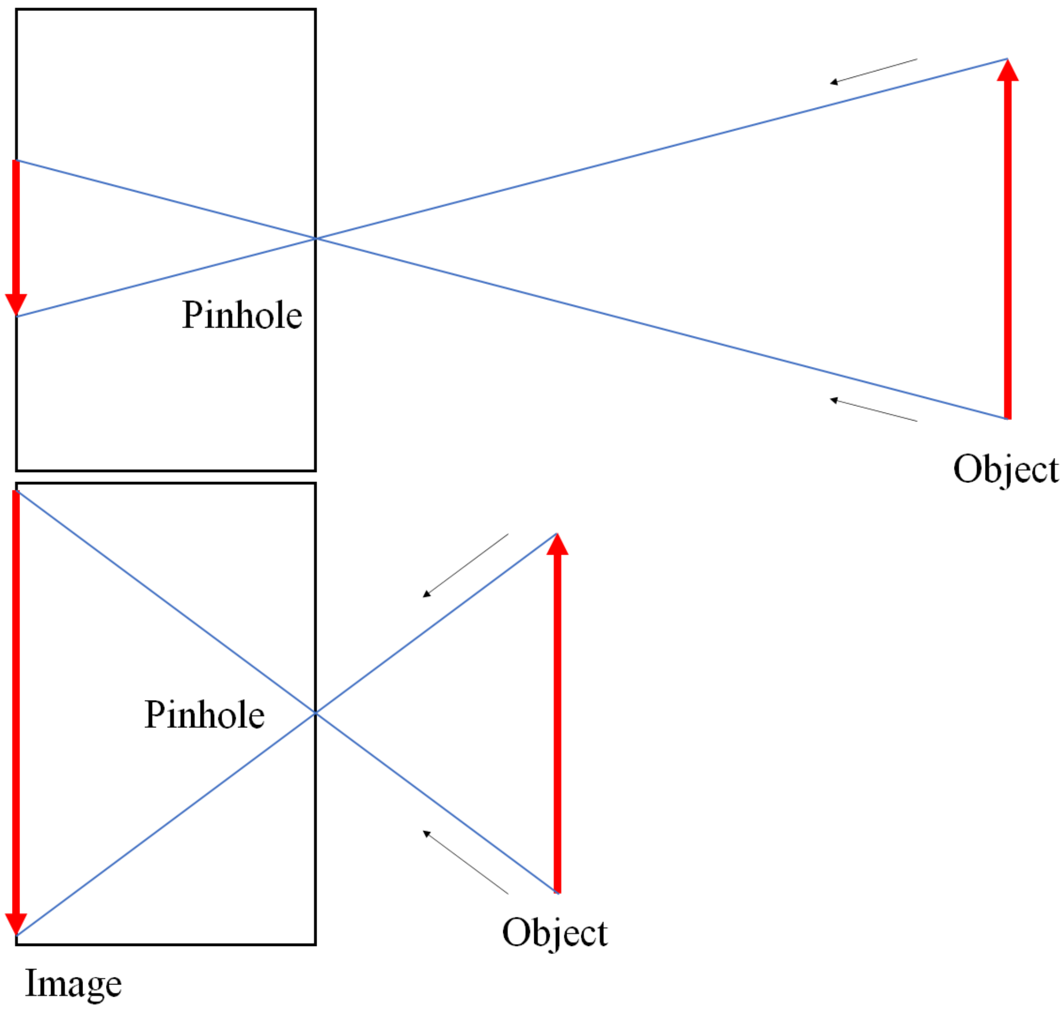

Figure 4.1 Principle of a pinhole camera with image at different distances of the object from the pinhole.

A tiny pinhole generally produces sharper images than a larger one. However, if the pinhole is too small, light waves may be scattered slightly at the edges of the pinhole and cause distortion or loss of focus. Smaller holes also increase exposure times since they let less light into the camera. Figure 4.2 shows the viewing angle for the pinhole camera. The viewing angle changes as we change the distance between the pinhole and the film or image sensor. Thus, this distance also is essential to determine the viewing angle of the pinhole imaging system.

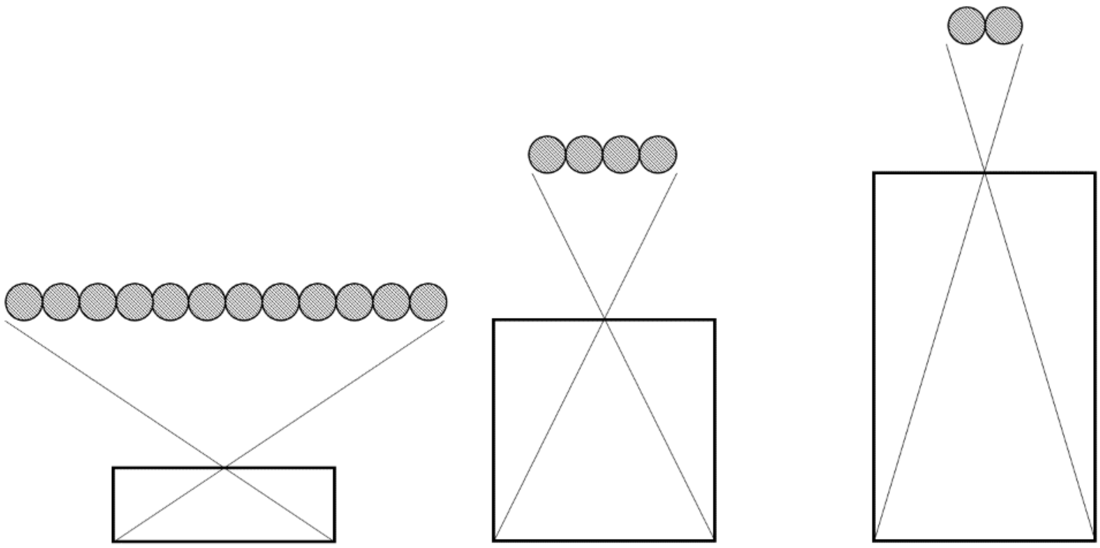

Figure 4.2 Viewing angle of the pinhole camera with different distances between pinhole and image plane.

4.1.2 FOD System, Principle, and Mechanism

Figure 4.3 depicts the system architecture of the FOD pinhole imaging technology. Based on Figure 4.3, the pinhole arrays were created at the OLED panel utilizing opaque materials like metals or black matrix materials. Separately created and connected beneath the OLED display were the OPD arrays for the imaging sensors. The OLED panel is used to illuminate the fingerprint surface to begin the fingerprint reading process. Then, the light will pass through the pinholes after being reflected from the fingerprint surface. The OPDs located beneath the OLED panel will then read the passing-through lights. As illustrated in Figure 4.4, the sectional view shows how the ridges and valleys reflect the light from the OLED panel to the pinhole. Due to different patterns of ridges and valleys in the fingerprint surface, the reflected light intensity will also differ. Thus, the OPDs underneath the OLED panel sense the reflected light and identify the fingerprint pattern through the image processing technique.

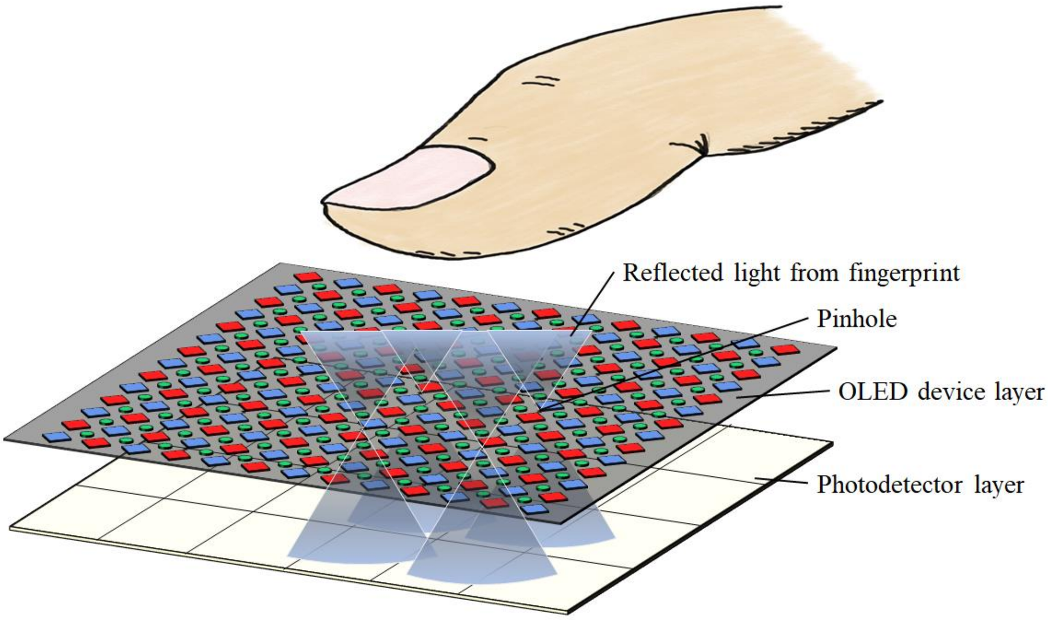

Figure 4.3 System architecture of FOD application.

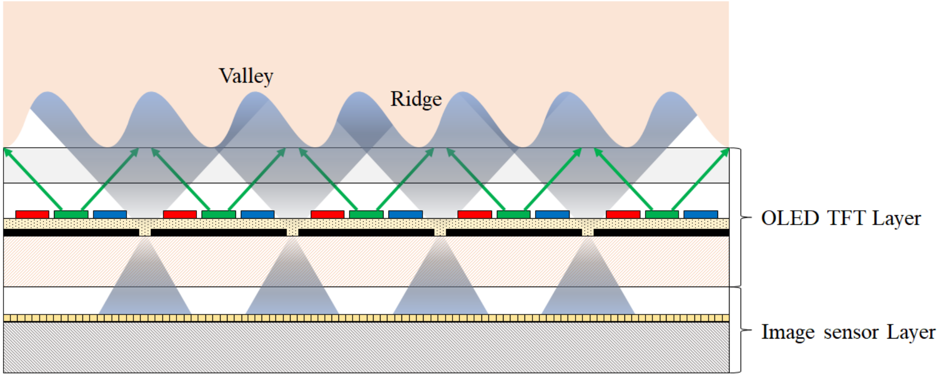

Figure 4.4 Principle of FOD from the pinhole sectional view.

4.2 ANALYSIS MODELING

Figure 2 depicts the constructed system employed in this analysis, which comprises only the most essential parameters to keep things simple. This model assumes a pinhole and Lambertian reflection from the fingerprint surface and employs a simple pinhole camera system.

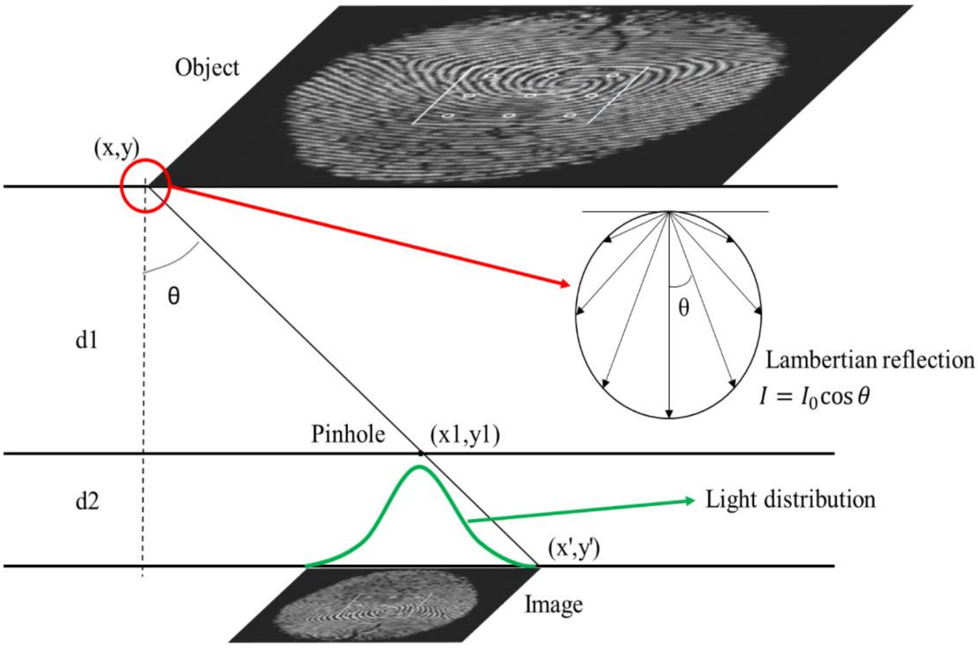

Figure 4.5 Pinhole imaging model based on the Lambertian reflection and pinhole system.

Here, *d1* corresponds to the thickness of the cover glass. At the same time, *d2* represents the distance between the pinhole and the OPD surface. It considers the thickness of the OLED substrate and the OPD's lamination layer. The light distribution on the sensor surface is calculated using Equation (4.1), derived from the Lambertian reflection equation.

$$
\begin{aligned}
I &= I_0 \cos\theta \\
&= I_0 \frac{d_1}{\sqrt{(x-x_1)^2+(y-y_1)^2}},
\end{aligned}
\tag{4.1}
$$

where (x, y) is the edge of the object, (x_1, y_1) represents the location of the pinhole. Based on this equation, the projected image is shrunk by the ratio of d_2/d_1.

4.3 RESULTS AND DISCUSSIONS

In this analysis, we tried to analyze the light distribution from the pinhole to the image sensor. It is crucial as it can help reduce the optical crosstalk between neighboring pixels for the image sensor and further increase the resolution of the image sensor. Thus, we can achieve a robust and reliable fingerprint sensor. Here, we used three pinholes with a 1 mm pitch size. The $d1$ and $d2$ values were fixed at 500 µm and 100 µm, respectively.

4.3.1 Light Distribution from Pinholes

The distribution of light intensity from three pinholes onto the sensor's surface is shown in Figure 4.6. The area beneath the pinhole had the highest light intensity on the sensor surface. The light intensity decreased as the sensor point moved away from the center. Other pinholes showed a similar pattern. The overlapped light intensity distribution from various pinholes is also shown in Figure 4.6. One optical crosstalk source that needs to be properly addressed is the high light intensity at the overlapped area. This optical crosstalk will give incorrect information throughout the biometric recognition process, lowering the system's dependability.

Decreasing the sensor pixel size is one method for reducing this optical crosstalk. As seen in Figure 4.6, it can be carried out based on the distribution of light intensity at the effective region. According to the Federal Bureau of Investigation (FBI), the standard for a biometric authentication system's minimum resolution must be 500 pixels per inch (ppi).[87)] Based on this specification, a minimum resolution of 50 μm is required for a reliable system. It means that for every 1000 μm, at least 20 pixels are necessary for such a system. Our analysis used a 200 μm sensor size with 10 μm per pixel.

As depicted in Figure 4.6, the diffraction might be anticipated in this system, as we can observe since we are only considering the simplicity of the analysis by taking care only of the *d1*, *d2*, and pinhole's pitch. This system can be improved by considering additional factors like pinhole diameter and thickness. Where diffraction occurs naturally, it is crucial for a lensless imaging approach. We can enhance the image's sharpness and resolution by reducing the pinhole size to as small as possible. However, the propagated light via the pinhole will induce spreading owing to diffraction as it gets smaller, on the other hand. Nevertheless, we can enhance this system by considering pinhole geometry, such as the diameter size and thickness. In addition, the diffraction and internal interference within the structure due to the small pinhole's size need to be addressed to avoid system vulnerability.

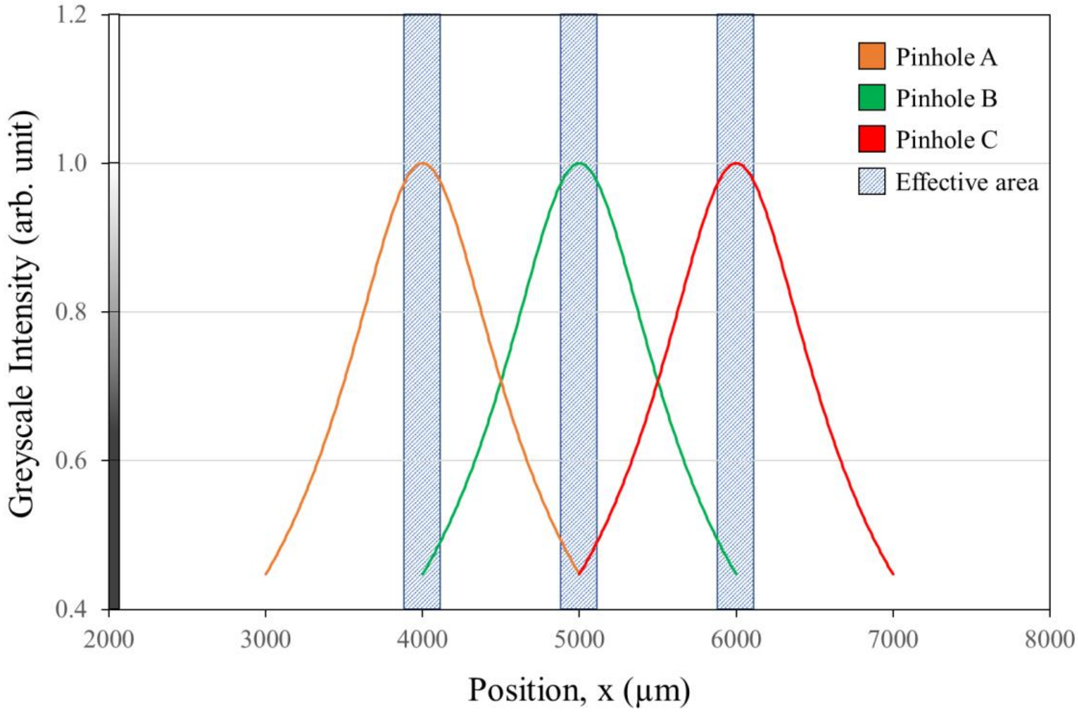

Figure 4.6 Light intensity distribution between neighboring pinholes.

4.3.2 Fingerprint Image Analysis

Most of the current commercial Automated Fingerprint Identification Systems (AFIS) rely primarily on Level 1 and Level 2 features and 500 ppi photos as their starting point. However, Level 3 features are required due to the increasing requirement for a reliable latent fingerprint or palm inspection. It has the support of the forensic community and adheres to FBI standards.[87)] Despite the Level 2 features having enough details, such as ridge bifurcations and endpoints, Level 3 features add more ridge characteristics, including pores, wrinkles, warts, and scars.

We also tried to observe the impact of several pinholes on the imaging system. The fingerprint image was processed based on the pinhole imaging analysis, as shown in Figure 4.7. We started with the initial fingerprint image in Figure 4.7(a), which displays the complete picture. We used nine pinholes for the image analysis on the entire fingerprint image. The processed images from nine separate pinholes are displayed in Figure 4.7(b). Since this is one of the features of the pinhole camera system, each pinhole that produces fingerprint pictures was rotated and reversed. We can note the apparent differences between ridges and valleys in the final image processing, shown in Figure 4.7(c), following the stitching process from each pinhole. As this image only has Level 1 features, it is still insufficient. Therefore, further pinhole configuration is necessary to increase the resolution to be a reliable system for the FOD system.

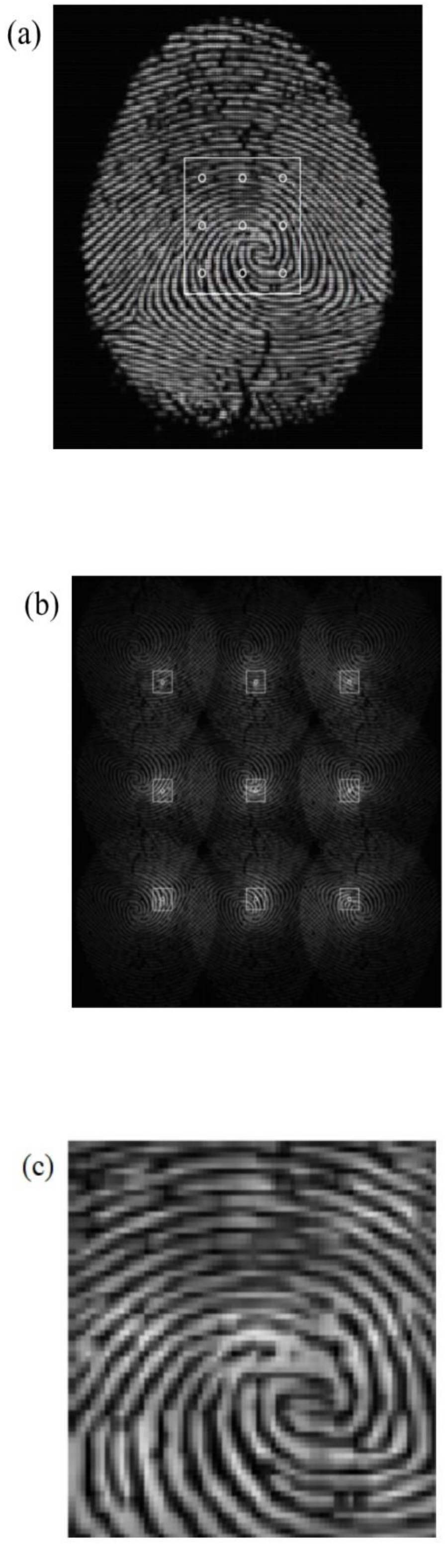

Figure 4.7 Pinhole's imaging analysis onto fingerprint image.

4.4 SUMMARY

In conclusion, we looked at the FOD structure using the pinhole imaging approach. The investigation was carried out to demonstrate the impact of pinholes on the dispersion of light across the sensor surface. Optimization is required to increase the system’s future reliability and capability. The trade-off between the pinhole’s geometry and diffraction is a crucial variable that needs to be considered for future improvement. In this analysis, we can reduce the optical crosstalk between the sensor’s pixels by choosing the sensor size based on the light distribution.

CHAPTER V

INTERDIGITATED ELECTRODES STRUCTURE OF OPD

5.1 INTRODUCTION

Our daily lives have been significantly impacted by the emergence of the digital and information ages, particularly using smartphones and fast internet. This technology is mainly utilized for social and personal communication, entertainment, financial data access, and online shopping. After that, the complete front-side display, which has recently dominated the market, also evolved in smartphone design. Thus, most smartphones have eliminated the traditional capacitive fingerprint sensor, often found in the bezel or home button, to increase the display-to-phone size ratio.

As discussed in Chapter IV, the biometric authentication system should at least have a minimum resolution of 500 ppi.[13),88),89)] Under this specification, the pixel size for the image sensor will be around 50 µm at maximum, and it should decrease further as the resolution increase beyond 500 ppi. Realizing biometric recognition throughout the display area has been attempted numerous times. For the fingerprint recognition system, one used a hybrid organic-inorganic thin-film photodetector.[83)] Other researchers have shown how to move from the construction of fingerprint sensors utilizing the OPD to vein detection and later integration with a display for biometric recognition.[13),51),84)] The pinhole imaging technique's use for FODs has only been the subject of several investigations. The fingerprint picture was obtained by incorporating a flexible active-matrix organic light-emitting diode (AMOLED) panel.[85] The Moiré pattern effect has also been the subject of additional research using this imaging technique for this application.[86] There is still a lack of knowledge regarding the optical crosstalk between pixels for the organic image sensor, even though numerous researchers have successfully recognized fingerprints utilizing OPDs. This issue is crucial because system crosstalk could result in inaccurate fingerprint authentication information. Additionally, pinhole imaging seems to have a lot of potential for streamlining the FOD system. However, interference and diffraction are two fundamental issues with the pinhole system that could lead to false readout results. Thus, a thorough analysis is needed to improve the authentication process.

5.2 DESIGN AND LAYOUT

We examined the diffusion photocurrent between nearby OPDs in this work. Using the interdigitated electrodes (IDEs) structure, this technique estimates the optical crosstalk between adjacent pixels in the organic image sensor. Here, we used the spin-coating method to deposit the solution-processable photoactive layer for OPD devices, further simplifying the procedure. However, it will create a continuous photoactive layer throughout the entire region. Therefore, there is a possibility that photocurrent diffusion between adjacent electrodes will occur.

Nevertheless, one drawback of the OSC is the short diffusion length of excitons. The small diffusion length, in the 5 – 10 nm range of the organic compounds employed in OPDs, is well recognized.[90)–93] Very few investigations have demonstrated the extraordinarily long diffusion length in the 2 – 8 μm range.[94,95] Despite that, we can fully utilize this drawback as an advantage. We can increase the number of pixels and, at the same time, decrease the pixel pitch length. It is possible to raise the resolution of the organic image sensor without going through a complicated patterning process for the active layer of the organic image sensor device.

5.2.1 IDE Layout Design

We tried to investigate the photocurrent crosstalk between neighboring pixels through the IDE structure. Figures 5.1(a) and 5.1(b) show the photomask for the covered layer, which is the Molybdenum (Mo), exposed area, and the transparent Indium-Tin-Oxide (ITO) layer. We used this structure to analyze the photocurrent diffusion from the exposed area to the covered electrodes. We changed the covered length (a µm) and distance between electrodes (b µm) based on Table 5.1.

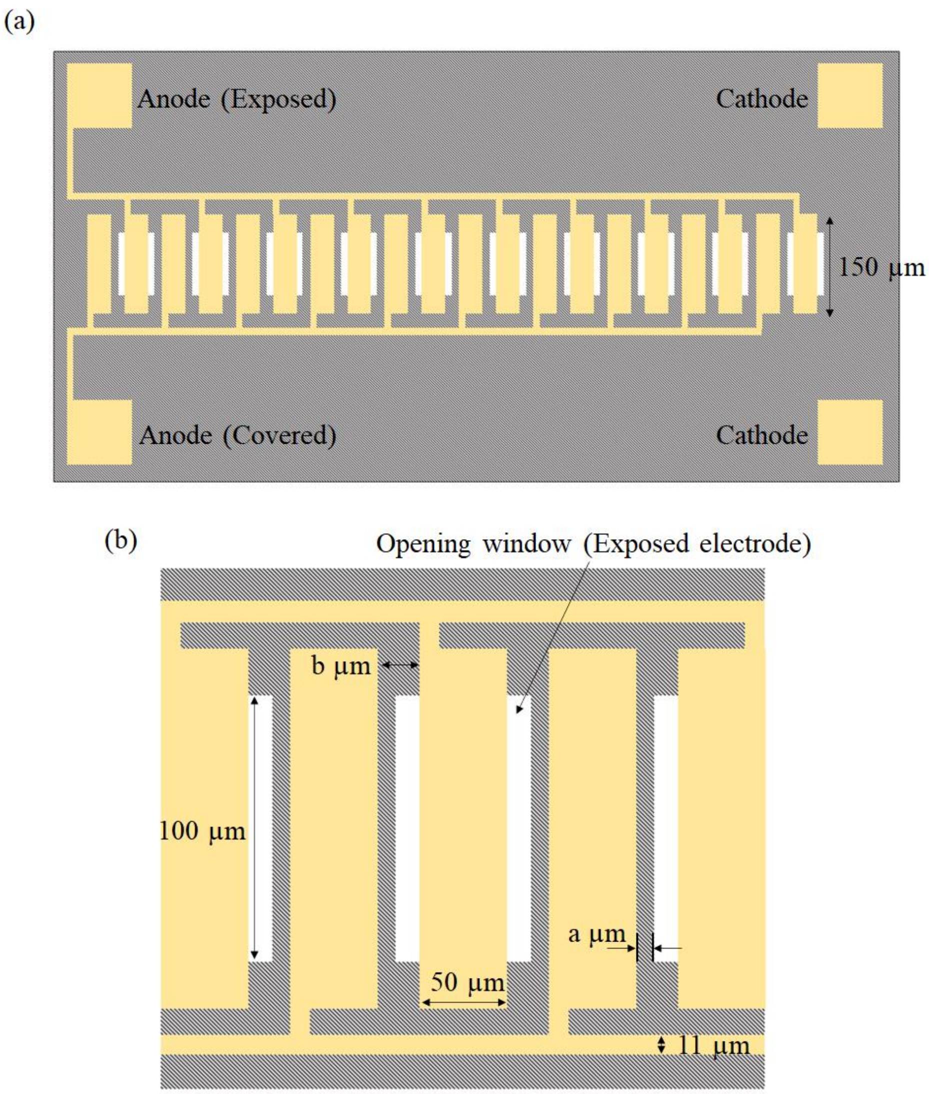

Figure 5.1 The IDE OPDs. (a) Overview of the photomask, and (b) closed-up view at the finger electrodes.

Table 5.1 Combinations of covered length and distance between electrodes.

Covered length a (μm)	**Distance between electrodes b (μm)**
10	20
5	10
2	4
1	2

This structure is challenging, especially in controlling the alignment between the electrodes and the opening windows. Therefore, we made several layouts with various alignment positions. We designed only one sample for each set that perfectly aligned the opening window and the exposed electrodes. We also created the other samples in each group to be intentionally shifted. The maximum shift for each set was equal to the distance between electrodes. We controlled the accuracy by changing the shift length with 1.0 μm, 0.5 μm, 0.2 μm, and 0.1 μm for 10 μm, 5 μm, 2 μm, and 1 μm, respectively. The layout of the designs is shown in Appendix A.

5.2.2 IDE OPD Fabrication Process and Characterization

The empty glass substrates were cleaned with acetone, isopropyl alcohol (IPA), and water in 5 min ultrasonic treatments. The substrates were dried, and DC magnetron sputtering was used to deposit Mo for a thickness of 100 nm. Photolithography and wet etching processes were used to create the patterns. For the IDE OPDs, the Mo layer serves as a built-in shadow mask. Afterward, a 200 nm thick SiO_2 isolation layer was formed using plasma-enhanced chemical vapor deposition (PECVD). This layer separates the shadow mask layer from the OPD device electrically. The transparent anode was created by creating a 100 nm ITO layer through DC magnetron sputtering and then patterning it with photolithography and wet etching. The negative photoresist (negative PR) was employed as an isolation layer between other IDE OPDs on the same substrate by spin-coating and patterning.

The poly(3-hexylthiophene-2,5-diyl) (P3HT) and [6,6]-phenyl C_{61}-butyric acid methyl ester (PCBM) were dissolved in chlorobenzene (CB) without additional purification to create the bulk-heterojunction (BHJ) of photoactive material. The concentration of the combination was 10 mg/mL, with a fixed mass ratio of 1:1, and it was ultrasonicated for 30 minutes. Afterward, the pre-patterned ITO substrates were exposed to UV-ozone for 15 minutes. As the hole transport layer (HTL), the poly(3,4-ethylenedioxythiophene): poly(styrene sulfonate) (PEDOT: PSS) solution was spin-coated on the substrates and annealed at 160°C for 10 min. The spin-coating procedure was used to deposit the P3HT: PCBM blends onto the PEDOT: PSS layer. Then, the samples were annealed for 10 min in an N_2 atmosphere at 100°C. Finally, a cathode layer of Aluminum (Al) was created using a thermal evaporation technique with a thickness of 70 nm. Figures 5.2(a) and 5.2(b) show a sectional view of the entire created IDE OPDs structure.

After ITO patterning, the optical microscope was used to locate the correctly aligned device within each set. After the fabrication process was completed, only the suitably aligned devices were characterized. The device's current density-voltage (*J*-*V*) properties were measured at room temperature using a parameter analyzer (Agilent 4156C Precision Semiconductor Parameter Analyzer). We tested the devices in dark and illuminated conditions. For both circumstances, the exposed and covered electrodes were simultaneously biased with the same voltage. By adjusting the provided current to the LED, a commercially available red-green-blue (RGB) LED with a wavelength of 525 nm was utilized to illuminate the IDE OPDs from the bottom side with varying irradiation strengths. A commercially available Si photodiode was used to assess the light intensity of the light source.

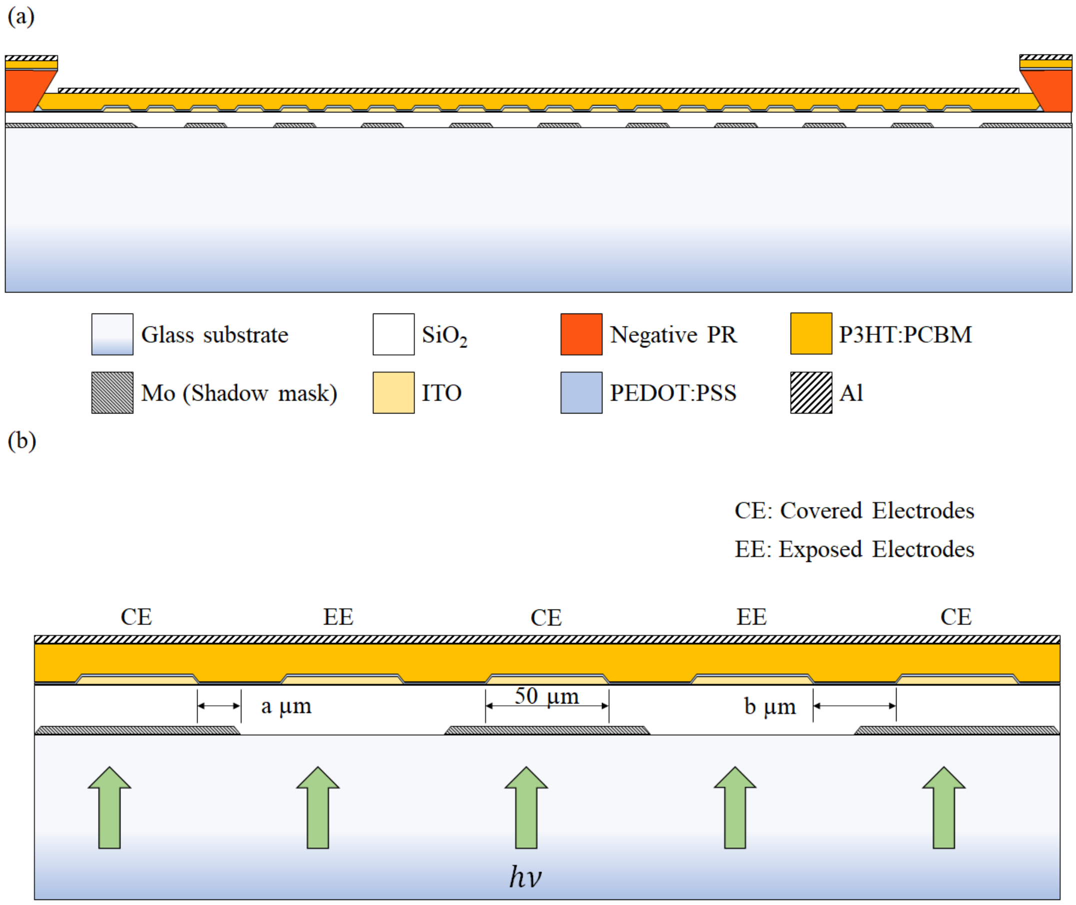

Figure 5.2 The sectional view of the bottom-side illumination IDE OPDs. (a) Overview of the IDE OPDs, and (b) closed-up view of the IDE OPDs at the covered and exposed electrodes.

5.3 *J-V* CHARACTERISTICS OF THE IDE OPD DEVICES

The fabricated IDE OPDs were used to test photocurrent diffusion between electrodes. As indicated in Table 5.1, previously, we sought to examine the diffusion length by varying the distances between electrodes. The spin-coating method was presented in which the PEDOT: PSS and P3HT: PCBM layers are shared between each electrode. Despite the simplicity of the spin-coating technique, this study is required to estimate the optical crosstalk between neighboring pixels for the organic image sensor, notably for the biometric authentication system in display technology.[85),86)] Measuring the diffusion photocurrent or crosstalk between pixels, especially from a single-pixel sensor, is extremely difficult. As a result, based on the accumulated current from each covered electrode, we employed the IDE structure to measure photocurrent diffusion from the exposed area to the covered electrodes.

The fabricated device for each procedure with the smallest feature size from Table 5.1 is shown in Figure 5.3. The photos on the left offer an overview of the IDE OPDs. In contrast, the ones on the right show a close-up look at the electrodes. As discussed in the experimental setup, the electrodes and shadow mask alignment were used to control the accuracy. Figures 5.3(a) and 5.3(b) show the pre-patterned ITO layer. Then, the deposited PEDOT: PSS layer on the sample is shown in Figures 5.3(c) and 5.3(d) through the spin-coating technique. Later, as illustrated in Figures 5.3(e) and 5.3(f), the P3HT: PCBM blend was deposited using the same method. Finally, as described in Figures 5.3(g) and 5.3(h), the Al cathode layer is deposited using the thermal evaporation method. The optical inspection of the constructed device reveals no anomalies and comparable findings on additional devices on the same substrate.

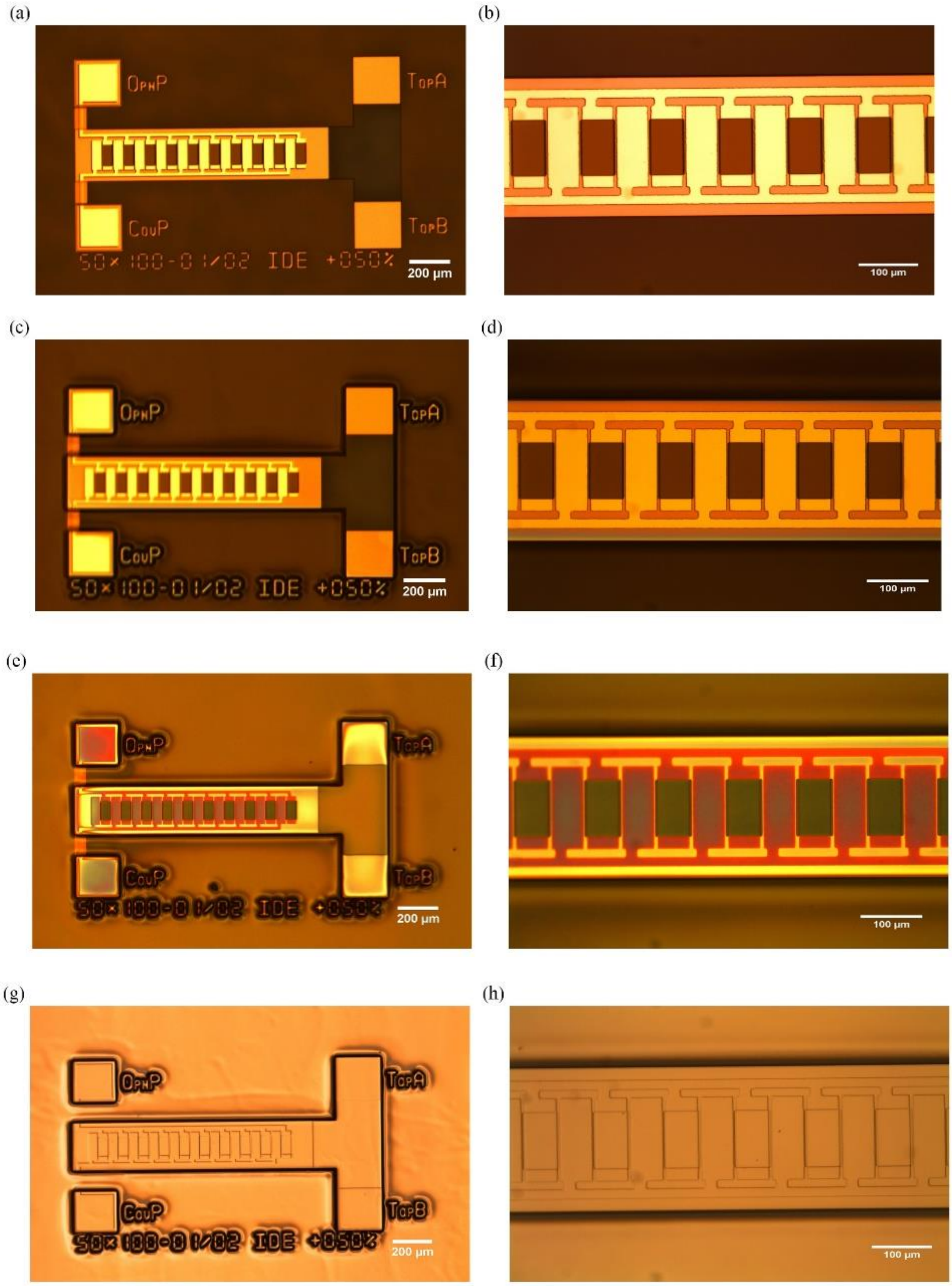

Figure 5.3 Optical microscope inspection of the IDE OPDs with 1 µm distance. Overview (left) and closed-up (right) view at the electrodes for each process. (a)-(b) Pre-patterned ITO. (c)-(d) PEDOT: PSS deposition. (e)-(f) P3HT: PCBM deposition. (g)-(h) Al cathode deposition.

In the dark and illumination conditions, Figure 5.4 depicts the current density-voltage (*J*-*V*) characteristics of the IDE OPDs between the exposed and covered electrodes for all configurations based on Table 5.1. For all structures at -1 V, the average dark current density, J_d, was 5.38×10^{-6} A/cm^2 to 6.75×10^{-5} A/cm^2 for exposed electrodes and 5.38×10^{-6} A/cm^2 to 2.36×10^{-5} A/cm^2 for covered electrodes. It demonstrates that all devices have the same J_d range. Figure 5.4 shows these IDE OPDs were also evaluated at various optical powers. The exposed electrodes demonstrate an acceptable ON/OFF ratio for a low incident optical power at -1 V at all device configurations. The current density under illumination increased by two orders of magnitude as the optical power increased to 60 W/cm^2.

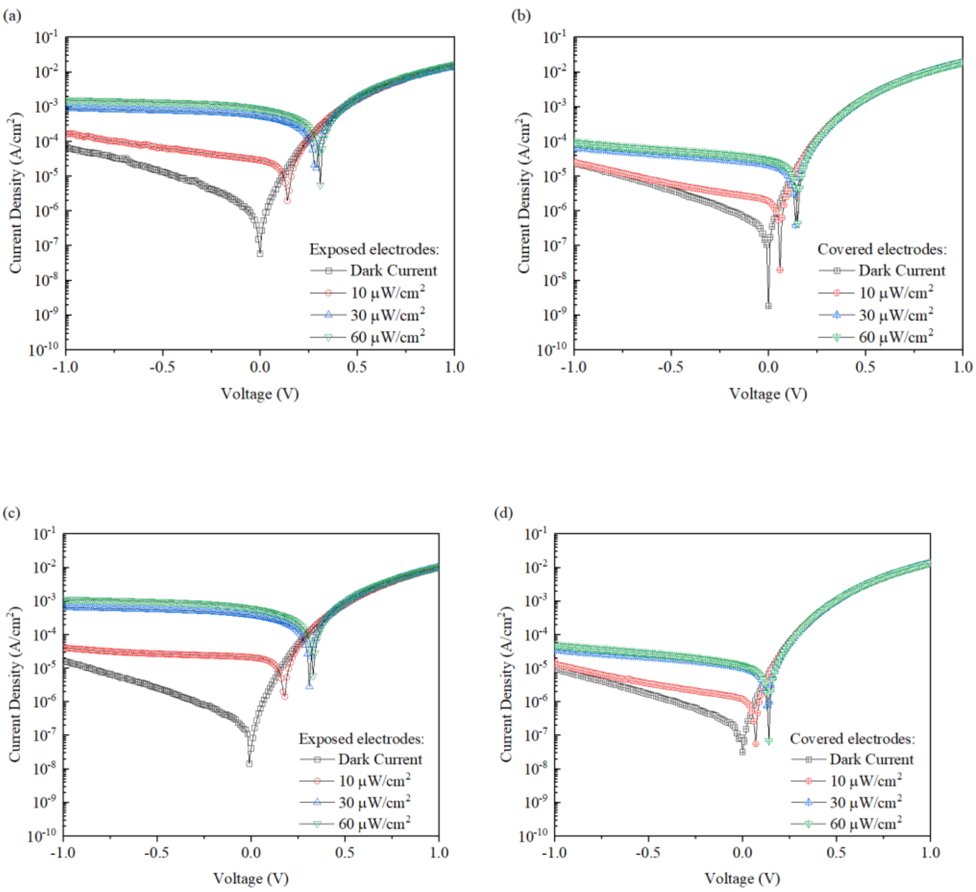

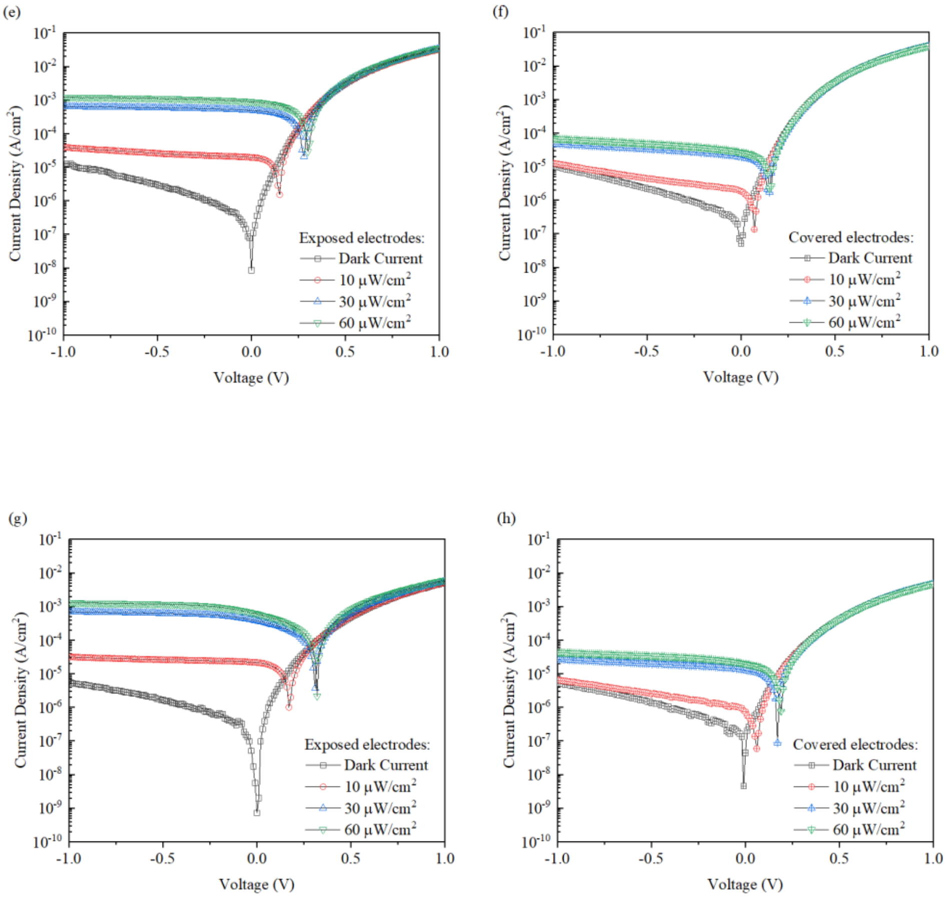

Figure 5.4 *J-V* characteristics of IDE OPDs for exposed (left) and covered (right) electrodes at different distances between covered ITO electrodes and exposed area. (a)-(b) 10 μm, (c)-(d) 5 μm, (e)-(f) 2 μm, and (g)-(h) 1 μm.

Surprisingly, even for the 10 μm length, the photocurrent change under illumination was seen for the covered electrodes. We hypothesized that during irradiation, the excitons (bounded electron-hole pairs) from the exposed area were diffused to the covered electrodes via the P3HT: PCBM layer. Even if photocurrent from reflected light is possible, we may presume it will be insignificant in this scenario. One of the reasons is the efficiency of absorbance for the P3HT: PCBM at 500 nm wavelength region. Most studies show that the absorbance of this blend layer for 100 nm thickness is roughly 80% within the 500 nm to 550 nm wavelength range.[16)–21)] In addition, it has a very low transmittance of less than 30%.[94)] As a result, in this analysis, the internal reflection from the Al top contact cathode is considered insignificant. We used a thin-film structure to fabricate the device, with an OPD total thickness of less than 1 µm and a gap between the OPDs and the shadow mask of roughly 200 nm based on SiO_2 thickness. Most of the light will reach the top cathode layer through the opening windows. The reflected light from the cathode layer has a reduced angle due to the thin-film structure, limiting the odds of illuminating the covered electrodes. As a result, the traveling light of the horizontal layer in our investigation may be minimal.

We next used Equation (5.1) to obtain the photocurrent density, which we used to examine the J-V characteristics further:

$$J_{ph} = J_{ill} - J_{d}, \tag{5.1}$$

where J_{ph}, J_{ill}, and J_{d} denote the photocurrent density, illuminated current density, and dark current density, respectively. Figure 5.5 depicts the J_{ph} of the IDE OPDs between the exposed and covered electrodes from 0 V to -1 V. We also included the J_{d} as the reference for each graph. For all designs, the J_{ph} of the exposed electrodes at -1 V is greater than that of the covered electrodes. Similar observation at the lowest light intensity used in this measurement which is 10 W/cm^2. For 10 W/cm^2, the hidden electrodes had a lower J_{ph} than the exposed electrodes, down to one order of magnitude. As the light intensity increased, the J_{ph} for the covered electrodes grew by two orders of magnitude. For the exposed electrodes, it was, however, practically at the same J_{ph} level at 10 W/cm^2. The Poole-Frenkel effect caused a modest increase in the J_{ph} as the reverse-biased voltage was increased.[96),97)]

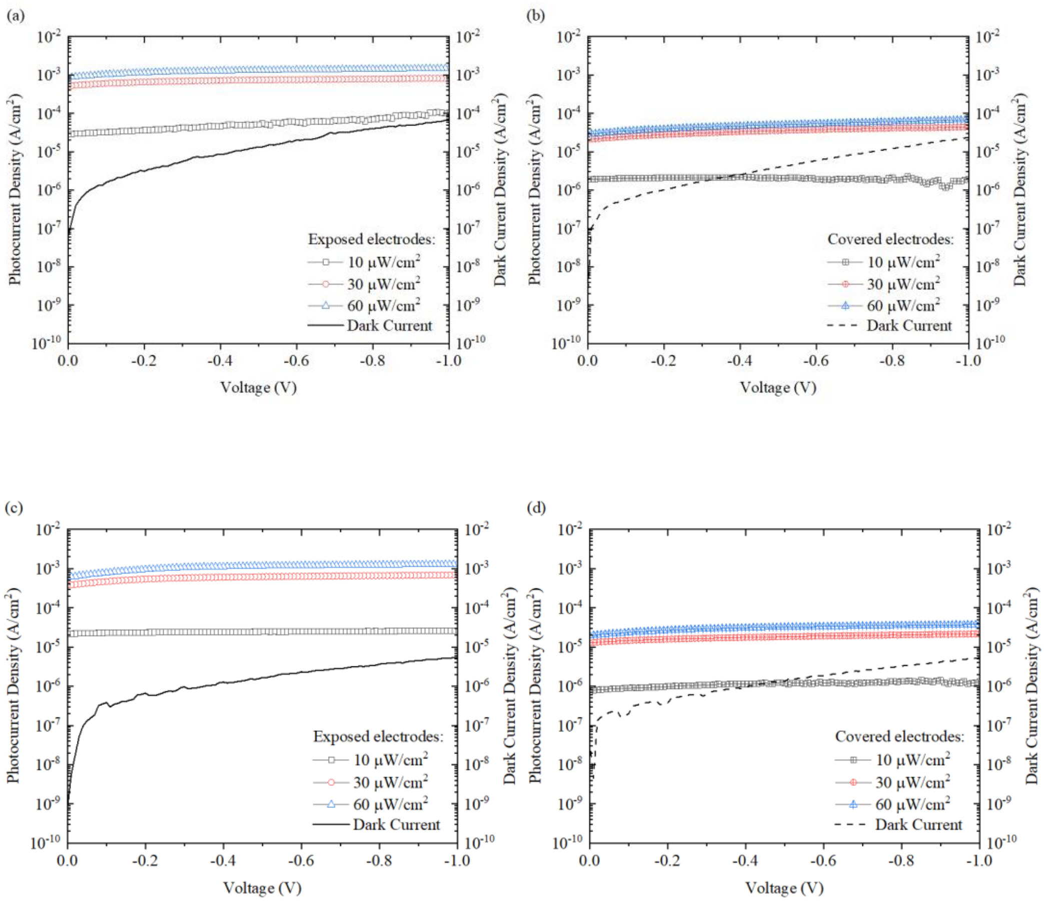

Figure 5.5 Photocurrent density of exposed (left) and covered (right) electrodes for (a)-(b) 10 μm, and (c)-(d) 1 μm.

Table 5.2 summarizes the J_{ph} retrieved from the measurement under various light intensity settings for all devices with multiple configurations, as described in Table 5.1. The J_{ph} of hidden electrodes is lower than the exposed electrodes at all light intensities employed. As a result, we can choose a cut-off biasing voltage for exact fingerprint detection. For both 10 µm and 1 µm distances at -1 V and a light intensity of 10 W/cm^2, the J_{ph} of the exposed device is substantially more significant than the covered device at -1 V.

Table 5.2 Summarized photocurrent density for the IDE OPDs.

Optical Power (µW/cm^2)	**Photocurrent Density @ -1 V (A/cm^2)**							
	Covered Length							
	1 µm		**2 µm**		**5 µm**		**10 µm**	
	Exposed	Covered	Exposed	Covered	Exposed	Covered	Exposed	Covered
10	2.6×10^{-5}	1.3×10^{-6}	2.6×10^{-5}	2.4×10^{-6}	2.5×10^{-5}	6.0×10^{-6}	1.0×10^{-4}	2.6×10^{-6}
30	6.9×10^{-4}	2.2×10^{-5}	6.3×10^{-4}	3.8×10^{-5}	6.2×10^{-4}	2.5×10^{-4}	8.2×10^{-4}	4.5×10^{-5}
60	1.3×10^{-3}	3.7×10^{-5}	1.2×10^{-3}	5.8×10^{-5}	1.1×10^{-3}	3.8×10^{-5}	1.5×10^{-3}	6.9×10^{-5}

5.4 DIFFUSION PHOTOCURRENT ANALYSIS

The crosstalk photocurrent at the concealed ITO electrodes is plotted against the distances between the hidden electrodes and the exposed area to assess our findings further. As we go further away from the exposed area, Figure 5.6 demonstrates a nearly constant crosstalk photocurrent. This discovery can confirm our earlier hypothesis on the negligibility of light reflection from the top cathode and light propagation through the BHJ's thin coating to the concealed ITO electrodes. As it exhibits practically constant crosstalk photocurrent, such effects were less noticeable even when we decreased the distance between the covered ITO electrodes and the exposed portion. As the leading cause of our findings, we shall concentrate on the exciton lifetime in our talk. It then prompts us to discuss how excitons diffuse to the covered electrodes.

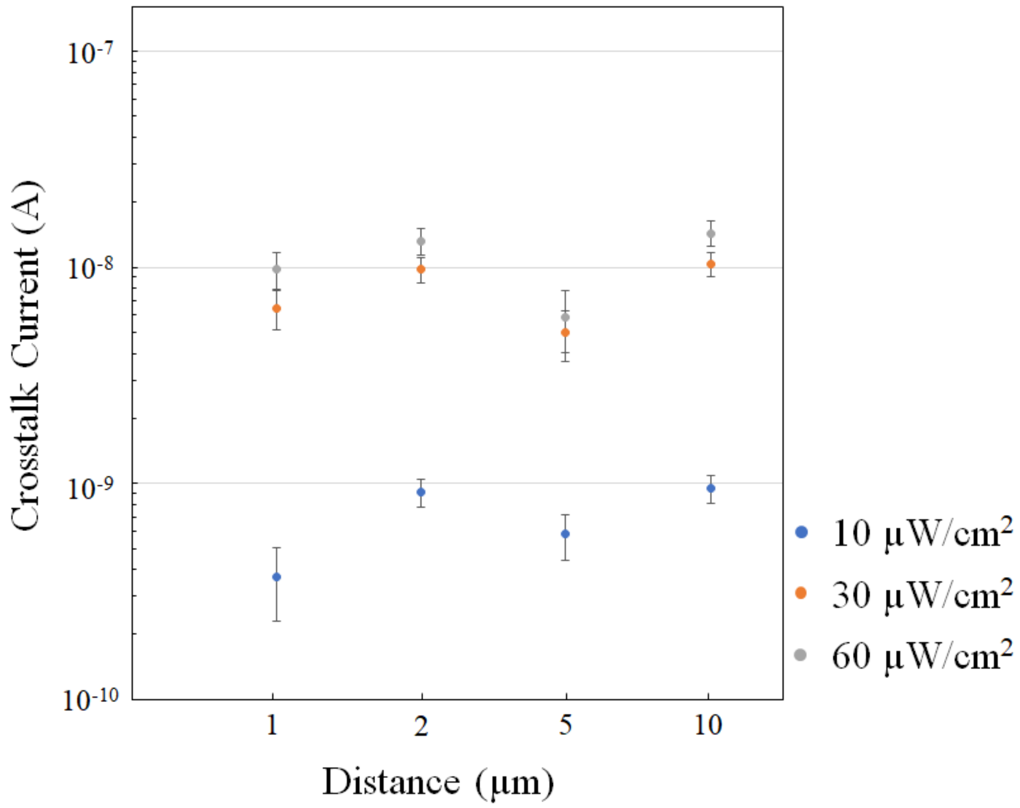

Figure 5.6 Crosstalk photocurrent for covered electrodes at different distances from the exposed area at different light intensities.

5.4.1 Long Exciton Lifetime

It is well known that OSC materials have an exciton diffusion length of between 5 and 10 nm.[90)–93)] Surprisingly, the J_{ph} was still discernible at a 10 μm between the hidden electrode and the exposed region. It might result from the shared HTL and BHJ layers on the entire surface. Excitons are initially produced by light absorption in the donor or acceptor materials. Within its lifetime (τ), it moves toward the donor-acceptor (D-A) interface, where effective charge separation occurs. The extent to which this migration happens also varies with the exciton diffusion length, L_D, in semiconductor materials. Following is a description of these L_D, where D represents the diffusion coefficient:[98)]

$$L_D = \sqrt{D\tau}. \tag{5.2}$$

Additionally, Figure 5.6 demonstrates that the distance had little to no effect on the crosstalk photocurrent. Equation (5.2) suggests that it could instead be connected to the lifespan of the exciton. In light of this, we propose that the extended exciton lifespan mainly caused the unexpectedly greater diffusion length.

The extended exciton lifetime that contributes to the unforeseen lengthening of the L_D can be explained by several processes, as we suggest. Before delving deeper into the long-lived excitons, we must first comprehend the BHJ layer utilized in our fabricated devices. The percolating networks of the D-A interfaces within the layer are formed by the molecular mixing of two distinct organic molecules that make up the BHJ structure. Due to variations in HOMO and LUMO levels between the D-A, an electrostatic force is produced at the D-A interface. If the energy is sufficient, these pairs can be separated to make free carriers once the created excitons are diffused to this interface. Otherwise, under a weak Coulombic limit, these excitons are relaxed to the charge transfer (CT) state. The ground and excited states are susceptible to this interaction between D-A and excitons. Because percolating networks also exist between the exposed and covered ITO electrodes, the D-A interaction between the excitons created in the exposed area and diffused to the covered area can still happen.

Within the course of their lives, these free-charge carriers will continue to diffuse. According to Onsager's theory, the free-charge carrier could escape the recombination due to their mutual Coulomb attraction and external electric field.[99)] Later, Braun strengthen Onsager's approach even more. He claimed that the recombined electron-hole (e-h) pairs could decay to the ground state or split into the free carrier with field dependence. Additionally, the charge carriers can reunite as a bound pair once separated. As a result, free carriers caught in bound pairs may dissociate over the bound pair's lifetime. Therefore, these long-lasting charge transfer states serve as a precursor for free charge carriers. It has been shown that after creation, bound e-h pairs in PPV: PCBM blends can still be identified after microseconds or even milliseconds.[100),101)] However, it still depends on the temperature. In our case, the area between the electrodes cannot be subjected to an external electric field. Then, we constantly illuminated the devices while measuring, but still under room temperature. Therefore, the long-lived excitons in the CT state can diffuse deeper to the nearby electrodes if this repeating process occurs during the lifetime. As a result, it increased the lifespan of the exciton, and unexpectedly prolonged L_D, as we observed in our devices based on Equation (5.2). Thus, we can assume that the diffuse e-h pairs in the CT state are one of the main factors that lead to photocurrent detection at the covered electrodes.

5.4.2 Exciton Diffusion

As can be seen in Figure 5.6, the crosstalk current at the covered ITO electrodes was observed despite the commonly known short L_D of the exciton. Therefore, we sought to examine the exciton diffusion by using Figure 5.7, and it can be expressed as follows:[98)]

$$\frac{\partial n}{\partial t} = D\frac{d^2 n}{dx^2} - \frac{n}{\tau} + G, \tag{5.3}$$

where the diffusion coefficient, exciton density, lifespan, and exciton generation rate are *D*, *n*, and *G*, respectively. Based on Equation (5.3), diffusion’s first term represents the exciton motion. The second and third terms are exciton generation via light absorption and exciton recombination. Then, for our construction at the exposed area, we applied the analytical photocurrent solution of Goodman and Rose as follows:[102)]

$$J_{ph(ex)} = qdG_{carrier\_ex}, \tag{5.4}$$

where $J_{ph(ex)}$, q, d, and $G_{carrier\_ex}$ are, respectively, the elementary charge, the thickness of the BHJ layer, the photocurrent density at the exposed ITO electrode, and the generation rate of the carriers at the exposed ITO electrode.

We can assume that the exposed electrodes follow the metal-insulator-metal (MIM) model. In this model, the exciton dissociation is controlled by the electric field, F, as follows:[103)]

$$F = \left(E_{HOMO\_D} - E_{LUMO\_A} - \Delta E\right) / qd\,. \tag{5.5}$$

Here, E_{HOMO_D}, E_{LUMO_A}, and ΔE stand for the donor's HOMO, the acceptor's LUMO, and the difference between the sums of the acceptor's LUMO and cathode Fermi level and the donor's HOMO. This electric field is necessary for the tightly coupled excitons to dissociate effectively. Variations in the donor and acceptor materials, electron affinities, and ionization potentials cause a quick charge transfer across the interface. Each electrode will collect the dissolved e-h pairs to their respective electrodes, which leads to the photocurrent. Therefore, we assumed that there is no restriction on, or at least minimal restriction on, recombination in the exposed ITO anode region. As a result, in this scenario, the carrier lifetime always outweighs the travel time. Not all excitons will split into free charge carriers and contribute to the photocurrent. As a result, $G_{carrier\_ex}$ will be lower than G_{exc_ex}, the actual rate of exciton formation at the exposed area. We can further reduce Equation (5.3) by assuming steady-state illumination at the edge of the exposed area to:

$$n_{ex\_o} = \tau G_{exc\_ex}, \tag{5.6}$$

where $n_{ex\ o}$, as depicted in Figure 5.7, represents the exciton density at the boundary.

On the other hand, the exposed region cannot collect dissociated charges without the ITO of the anode. According to the decay rate and lifetime of the e-h pairs, we can expect that most of the charge carriers produced here undergo recombination and generation. Due to the absence of exciton formation in the covered area in the CT state, the accumulated excitons there will create a gradient of exciton density between the exposed and covered areas. These excitons will begin to distribute to the covered area as a result. It is possible to approximate these diffused excitons to the covered area using Equation (5.3), where under steady-state conditions, no exciton creation takes place:

$$D\frac{d^2 n_{\mathrm{cov}}}{dx^2} = \frac{n_{\mathrm{cov}}}{\tau}. \tag{5.7}$$

Equation (5.7) can be stated as follows, considering Equation (5.2):

$$\frac{d^2 n_{\mathrm{cov}}}{dx^2} = \frac{n_{\mathrm{cov}}}{{L_D}^2}. \tag{5.8}$$

The differential equation from Equation (5.8) can then be solved to determine the exciton density profile, which can be stated as follows:

$$n_{\mathrm{cov}} = n_{ex\_o} \exp\left(-\frac{x}{L_D}\right), \tag{5.9}$$

where x is the distance from the boundary to the edge of the hidden ITO electrode and n_{cov} is the diffused exciton in the covered area. The scattered excitons will face the internal electric field and contribute to the photocurrent once they reach the edge of the buried ITO electrode. As previously mentioned, not all diffused excitons will be separated into free charge carriers and extracted to the appropriate electrodes. The sensitivity of the instrument itself will be the critical determining factor.

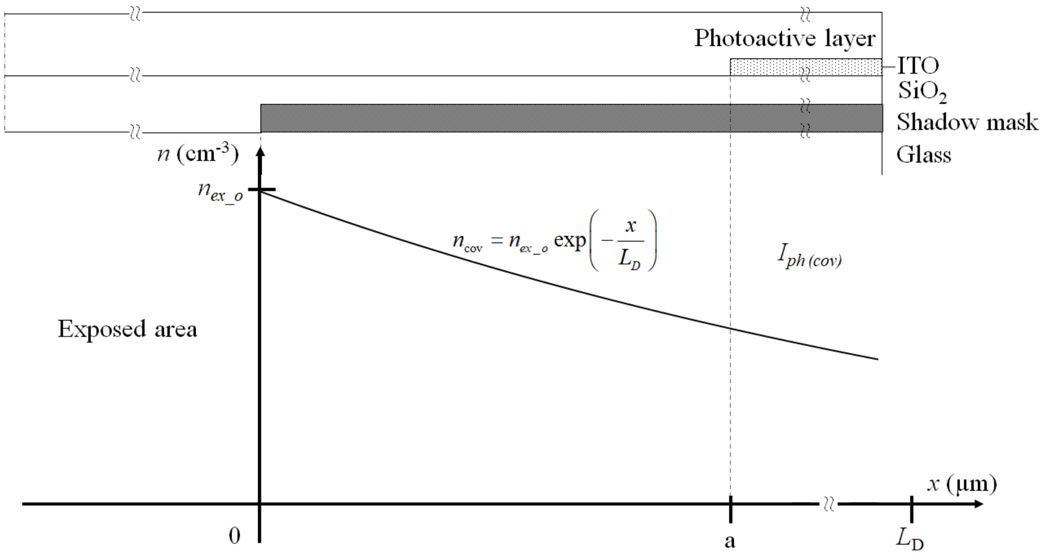

Figure 5.7 Exciton diffusion at the boundaries.

5.5 SUMMARY

In conclusion, using the constructed IDE OPDs structure, we showed how photocurrent diffused from the exposed part to the covered electrodes. Because it is straightforward and practical for the large-area sensor display, we constructed the device using the spin-coating method. Even though the L_D of OSCs is shorter than that of an inorganic semiconductor, we can detect the photocurrent at hidden electrodes for distances of up to 10 µm. In most instances, it conflicts with the widely accepted short L_D in the nanometer region. As we previously described, long-lived excitons are one of the factors that lead to the surprisingly long L_D. We also demonstrated that our devices were unaffected by the light's propagation or reflection inside the thin-film structure. Based on the finding, the photocurrent at the hidden electrodes at various distances had a similar order of magnitude. Except for the measured crosstalk photocurrent, our study has no direct information about the diffusion mechanism of the exciton motion in the horizontal direction based on our fabricated devices. According to our findings, we also propose that -1 V is the ideal device for biasing at low light levels to reduce the crosstalk effect between neighboring pixels. In addition, it can improve the device's accuracy for image-sensing applications. Even though the crosstalk photocurrent is already relatively low, it can be further decreased by appropriately isolating the device. It is achievable via lithography or inkjet printing, particularly for high-resolution image sensors.

CHAPTER VI

CONCLUSION AND FUTURE WORK

6.1 INTRODUCTION

In summary, we successfully attained the objectives of this study. Biometric authentication using OPD devices as the image sensor for the FOD system is proposed as the alternative to fulfill the demand for the full-display sensing application. The findings in this research are obtained and appropriately described according to the objective of the work. The conclusion to the main results is as follows:

a) The ray tracing analysis shows the behavior of the light propagation in the turbid media and how the structure gave the impact, especially for obtaining the PPG signal.

b) The light source and photodetector distance should be as close as possible for high PPG signal acquisition. In our simulation, the distance between the light source and detector must be less than 3 mm for the reflectance-based device.

c) The fingerprint images produced from the pinhole imaging technique show the feasibility of the FOD system, especially for the flat-panel display and thin-film device technology. The analysis performed in this study showed that the crosstalk that occurred from the adjacent pinholes was significantly high. In the case of the multi-pinhole system, we can further reduce the crosstalk by focusing on the sensor located underneath the pinholes based on the effective region.

d) The diffusion length analysis for the IDE OPDs structure shows unexpected results, which are longer than expected, where the photocurrent crosstalk was observed at 10 μm from the exposed to the covered electrodes.

e) The photocurrent crosstalk was observed at a 10 μm from the exposed area to the covered electrodes. Interestingly, an almost constant crosstalk photocurrent was observed at four different distances between the covered electrodes to the exposed area. One of the reasons we can deduce is the sharing of PEDOT: PSS and P3HT: PCBM layers throughout the whole surface of the fabricated devices.

6.2 OPTICAL PPG SENSOR ANALYSIS

Identity spoofing is a type of cyber assault that has occurred frequently, even though many authentication techniques are available. As technology advances, smartphones have become a significant part of our daily life, especially involving money transactions and identity access. One of the significant drawbacks of the optical biometric authentication approach is the use of fake fingerprints. Thus, PPG signal acquisition can help improve the system's security and reliability, especially for smartphone usage. Our simulation shows the behavior of the light propagated in the fingertip structure. For the reflectance-based principle, which will be mostly applied to the FOD system, the signal acquisition is feasible as most of the light from the display is usually very bright. Thus, there will be no issue regarding the light intensity to illuminate the fingertip structure. As we proposed the OPD as the image sensor used for fingerprint authentication, it can be used simultaneously to acquire the PPG signal for identity verification while using the system.

6.3 PINHOLE IMAGING ANALYSIS

The pinhole imaging for fingerprint authentication shows that it has the potential to be applied in future display technology. It can help to reduce the thickness by removing the lenses and collimators. It also helps to simplify the process for future display making. Even though pinhole technology has been around us for quite a long time, the application is still limited to only the camera itself.

6.4 CROSSTALK PHOTOCURRENT BETWEEN PIXELS

We used the IDE OPDs structure to analyze the crosstalk photocurrent between pixels for the biometric authentication system. The solution processed of OPDs can be used for the FOD system due to their simplicity. Even though the crosstalk photocurrent is already relatively low, it can be further decreased by appropriately isolating the device. It is achievable via lithography or inkjet printing, particularly for high-resolution image sensors.

6.5 FUTURE WORK AND RECOMMENDATION

Several improvements for the future and recommendations can be made to improve the system as follows:

- ❖ The ray tracing optical simulation can be further improved by analyzing the light propagation between the display, fingerprint surface, pinholes, and sensor. We can use this simulation to understand further how the structure can affect the PPG signal acquisition. We may further understand the behavior of the lights traveling within those structures. Thus, we can improve the system for its reliability.

- ❖ In the case of a pinhole system, we can further analyze the pinhole structures, such as the diameter and thickness. We can also explore how the distance between the pinholes might affect the system's image processing. Thus, we can improve the fingerprint image quality as our target is to follow the FBI standard for a robust design.

- ❖ As we were trying to propose the OPDs for the image sensor underneath the display for biometric authentication, a lot of work still needs to be done. We can proceed with several techniques, such as the proper isolation or blockage system between pixels so that the diffused exciton can be grounded elsewhere outside the sensing circuitry elements.

REFERENCES

1) A. K. Jain, A. Ross and S. Prabhakar, IEEE Trans. Circuits Syst. Video Technol. **14** [1], 4 (2004).
2) D. Bhattacharyya, R. Ranjan, F. Alisherov and C. Minkyu, Int. J. u- e- Service Sci. Tecnol. **2** [3], 82 (2009).
3) D. Maltoni, D. Maio, A. K. Jain and S. Prabhakar, Eds., *Handbook of Fingerprint Recognition* (Springer, London, 2009) 2nd ed.
4) S. Z. Li and A. K. Jain, *Handbook of Face Recognition* (Springer, London New York, 2011) 2nd ed.
5) A. K. Jain, A. Ross and S. Pankanti, in *Proceeding of 2nd International Conference on Audio- and Video-based Biometric Person Authentication (AVBPA)* (Washington D.C., 1999) pp. 1661.
6) J. Daugman, IEEE Trans. Syst., Man, Cybern. B **37** [5], 1167 (2007).
7) H. Ma, Z. Liu, S. Heo, J. Lee, K. Na, H. B. Jin, S. Jung, K. Park, J. J. Kim and F. Bien, IEEE Sensors J. **16** [22], 8124 (2016).
8) H. Hwang, H. Lee, B. Jang, H. Kim, T. Lee and Y. Chae, SID Symp. Dig. Tech. Pap. **48** [1], 838 (2017).
9) X. Jiang, Y. Lu, H.-Y. Tang, J. M. Tsai, E. J. Ng, M. J. Daneman, B. E. Boser and D. A. Horsley, Microsyst Nanoeng **3** [1], 17059 (2017).
10) S. Bae, Y. Ling, W. Lin and H. Zhu, SID Symp. Dig. Tech. Pap. **49** [1], 1017 (2018).
11) B. W. An, S. Heo, S. Ji, F. Bien and J.-U. Park, Nat Commun **9** [1], 2458 (2018).
12) G.-J. Jeon, S.-H. Lee, S. H. Lee, J.-B. Shim, J.-H. Ra, K. W. Park, H.-I. Yeom, Y. Nam, O.-K. Kwon and S.-H. K. Park, Sci Rep **9** [1], 3216 (2019).
13) D. Tordera, B. Peeters, H. B. Akkerman, A. J. J. M. Breemen, J. Maas, S. Shanmugam, A. J. Kronemeijer and G. H. Gelinck, Adv. Mater. Technol. **4** [11], 1900651 (2019).
14) K.-J. Baeg, M. Binda, D. Natali, M. Caironi and Y.-Y. Noh, Adv. Mater. **25** [31], 4267 (2013).
15) K. Kudo and T. Moriizumi, Appl. Phys. Lett. **39** [8], 609 (1981).
16) W. H. Lee, S. Y. Chuang, H. L. Chen, W. F. Su and C. H. Lin, Thin Solid Films **518** [24], 7450 (2010).
17) B. Hajduk, H. Bednarski, B. Jarząbek, H. Janeczek and P. Nitschke, Beilstein J. Nanotechnol. **9**, 1108 (2018).

18) L. Hrostea, M. Girtan, R. Mallet and L. Leontie, IOP Conf. Ser.: Mater. Sci. Eng. **374**, 012015 (2018).

19) H. Maruhashi, T. Oku, A. Suzuki, T. Akiyama and Y. Yamasaki, in *AIP Conference Proceedings* (Tsukuba-city, Ibaraki, Japan, 2015) Vol. 1649 pp. 89.

20) E. Zakhidov, M. Imomov, V. Quvondikov, S. Nematov, I. Tajibaev, A. Saparbaev, I. Ismail, B. Shahid and R. Yang, Appl. Phys. A **125** [11], 803 (2019).

21) F. L. Khairulaman, C. C. Yap and M. H. Hj Jumali, Mater. Lett. **283**, 128827 (2021).

22) T. Someya, Y. Kato, S. Iba, Y. Noguchi, T. Sekitani, H. Kawaguchi and T. Sakurai, IEEE Trans. Electron Devices **52** [11], 2502 (2005).

23) G. Simone, M. J. Dyson, S. C. J. Meskers, R. A. J. Janssen and G. H. Gelinck, Adv. Funct. Mater. **30** [20], 1904205 (2020).

24) M. Biele, C. Montenegro Benavides, J. Hürdler, S. F. Tedde, C. J. Brabec and O. Schmidt, Adv. Mater. Technol. **4** [1], 1800158 (2019).

25) M. Kielar, O. Dhez, G. Pecastaings, A. Curutchet and L. Hirsch, Sci Rep **6** [1], 39201 (2016).

26) X. Zhou, D. Yang and D. Ma, Advanced Optical Materials **3** [11], 1570 (2015).

27) A. Pierre, I. Deckman, P. B. Lechêne and A. C. Arias, Adv. Mater. **27** [41], 6411 (2015).

28) C. Xie, T. Heumüller, W. Gruber, X. Tang, A. Classen, I. Schuldes, M. Bidwell, A. Späth, R. H. Fink, T. Unruh, I. McCulloch, N. Li and C. J. Brabec, Nat Commun **9** [1], 5335 (2018).

29) F. J. M. Colberts, M. M. Wienk and R. A. J. Janssen, ACS Appl. Mater. Interfaces **9** [15], 13380 (2017).

30) J. Zhao, Y. Li, G. Yang, K. Jiang, H. Lin, H. Ade, W. Ma and H. Yan, Nat Energy **1** [2], 15027 (2016).

31) M. C. Scharber and N. S. Sariciftci, Progress in Polymer Science **38** [12], 1929 (2013).

32) Y. Huang, E. J. Kramer, A. J. Heeger and G. C. Bazan, Chem. Rev. **114** [14], 7006 (2014).

33) R. D. Jansen-van Vuuren, A. Armin, A. K. Pandey, P. L. Burn and P. Meredith, Adv. Mater. **28** [24], 4766 (2016).

34) A. Armin, R. D. Jansen-van Vuuren, N. Kopidakis, P. L. Burn and P. Meredith, Nat Commun **6** [1], 6343 (2015).

35) B. Siegmund, A. Mischok, J. Benduhn, O. Zeika, S. Ullbrich, F. Nehm, M. Böhm, D. Spoltore, H. Fröb, C. Körner, K. Leo and K. Vandewal, Nat Commun **8** [1], 15421 (2017).

36) S. Ullbrich, B. Siegmund, A. Mischok, A. Hofacker, J. Benduhn, D. Spoltore and K. Vandewal, J. Phys. Chem. Lett. **8** [22], 5621 (2017).

37) Z. Tang, Z. Ma, A. Sánchez-Díaz, S. Ullbrich, Y. Liu, B. Siegmund, A. Mischok, K. Leo, M. Campoy-Quiles, W. Li and K. Vandewal, Adv. Mater. **29** [33], 1702184 (2017).

38) M. R. Esopi, M. Calcagno and Q. Yu, Adv. Mater. Technol. **2** [8], 1700025 (2017).

39) N. Strobel, M. Seiberlich, R. Eckstein, U. Lemmer and G. Hernandez-Sosa, Flex. Print. Electron. **4** [4], 043001 (2019).

40) S. A. Choulis, J. Nelson, Y. Kim, D. Poplavskyy, T. Kreouzis, J. R. Durrant and D. D. C. Bradley, Appl. Phys. Lett. **83** [18], 3812 (2003).

41) G. Garcia-Belmonte, A. Munar, E. M. Barea, J. Bisquert, I. Ugarte and R. Pacios, Organic Electronics **9** [5], 847 (2008).

42) T. M. Clarke, C. Lungenschmied, J. Peet, N. Drolet and A. J. Mozer, Adv. Energy Mater. **5** [4], 1401345 (2015).

43) S. Kasap, J. B. Frey, G. Belev, O. Tousignant, H. Mani, J. Greenspan, L. Laperriere, O. Bubon, A. Reznik, G. DeCrescenzo, K. S. Karim and J. A. Rowlands, Sensors **11** [5], 5112 (2011).

44) G. A. H. Wetzelaer, M. Kuik, M. Lenes and P. W. M. Blom, Appl. Phys. Lett. **99** [15], 153506 (2011).

45) Th. Martin and R. Landauer, Phys. Rev. B **45** [4], 1742 (1992).

46) I. K. Kim, J. H. Jo, J. (Brian) Lee and Y. J. Choi, Organic Electronics **57**, 89 (2018).

47) G. H. Gelinck, A. Kumar, D. Moet, J.-L. van der Steen, U. Shafique, P. E. Malinowski, K. Myny, B. P. Rand, M. Simon, W. Rütten, A. Douglas, J. Jorritsma, P. Heremans and R. Andriessen, Organic Electronics **14** [10], 2602 (2013).

48) T. N. Ng, W. S. Wong, M. L. Chabinyc, S. Sambandan and R. A. Street, Appl. Phys. Lett. **92** [21], 213303 (2008).

49) C. Zhao, J. Kanicki, A. C. Konstantinidis and T. Patel, Med. Phys. **42** [11], 6294 (2015).

50) T. Kamada, R. Hatsumi, K. Watanabe, S. Kawashima, M. Katayama, H. Adachi, T. Ishitani, K. Kusunoki, D. Kubota and S. Yamazaki, J Soc Inf Display **27** [6], 361 (2019).

51) H. Akkerman, B. Peeters, A. Breemen, S. Shanmugam, L. Ugalde Lopez, D. Tordera, R. Ketterij, E. Delvitto, R. Verbeek, P. Malinowski, T. Ke, F. De Roose, L. Moreno Hagelsieb, I. Katsouras, A. J. Kronemeijer, E. Meulenkamp and G. Gelinck, J Soc Inf Display **29** [12], 935 (2021).

52) C. M. Lochner, Y. Khan, A. Pierre and A. C. Arias, Nat Commun **5** [1], 5745 (2014).

53) Y. Khan, D. Han, A. Pierre, J. Ting, X. Wang, C. M. Lochner, G. Bovo, N. Yaacobi-Gross, C. Newsome, R. Wilson and A. C. Arias, Proc. Natl. Acad. Sci. U.S.A. [DOI:10.1073/pnas.1813053115].

54) M. Gao, L. Li and Y. Song, J. Mater. Chem. C **5** [12], 2971 (2017).

55) Y. Dong, Y. Zou, J. Song, Z. Zhu, J. Li and H. Zeng, Nano Energy **30**, 173 (2016).

56) Z. Bao and X. Chen, Adv. Mater. **28** [22], 4177 (2016).

57) H. Lee, H. Ko and J. Lee, ICT Express **2** [4], 195 (2016).

58) E. D. Chan, M. M. Chan and M. M. Chan, Respiratory Medicine **107** [6], 789 (2013).

59) T. Tamura, Y. Maeda, M. Sekine and M. Yoshida, Electronics **3** [2], 282 (2014).

60) A. Caizzone, A. Boukhayma and C. Enz, IEEE Electron Device Lett. **40** [11], 1828 (2019).

61) A. Bilgaiyan, F. Elsamnah, H. Ishidai, C.-H. Shim, M. A. B. Misran, C. Adachi and R. Hattori, ACS Appl. Electron. Mater. **2** [5], 1280 (2020).

62) C.-Y. Huang, M.-C. Chan, C.-Y. Chen and B.-S. Lin, Sensors **14** [9], 17586 (2014).

63) F. Elsamnah, A. Bilgaiyan, M. Affiq, C.-H. Shim, H. Ishidai and R. Hattori, Biosensors **9** [3], 87 (2019).

64) M. Hiraoka, M. Firbank, M. Essenpreis, M. Cope, S. R. Arridge, P. van der Zee and D. T. Delpy, Phys. Med. Biol. **38** [12], 1859 (1993).

65) J. L. Reuss and D. Siker, J Clin Monit Comput **18** [4], 289 (2004).

66) V. A. Peris and S. Hu, J. Phys.: Conf. Ser. **85**, 012027 (2007).

67) S. Chatterjee and P. Kyriacou, Sensors **19** [4], 789 (2019).

68) K.-C. Huang, C.-L. Chang, H.-C. Chang and C.-H. Chang, in *2012 IEEE International Instrumentation and Measurement Technology Conference Proceedings* (IEEE, Graz, Austria, 2012) pp. 1246.

69) V. V. Tuchin, J. biomed. photonics eng. **1** [2], 98 (2015).

70) V. Tuchin, J. biomed. photonics eng. **2** [3], 030201 (2016).

71) I. V. Meglinsky and S. J. Matcher, Med. Biol. Eng. Comput. **39** [1], 44 (2001).

72) I. V. Meglinski and S. J. Matcher, Computer Methods and Programs in Biomedicine **70** [2], 179 (2003).

73) J. L. Latham and S. N. Martin, Am Fam Physician **89** [12], 956 (2014).

74) L. Jazayeri, J. Q. Klausner and J. Chang, Plast Reconstr Surg **132** [5], 1207 (2013).

75) C. Y. Chia and T. Nassif, Rev. Bras. Cir. Plást. **26** [4], 714 (2011).

76) C. Y. Chia and T. Nassif, Rev. Bras. Cir. Plást. [DOI:10.5935/2177-1235.2015RBCP0185].

77) A. N. Bashkatov, E. A. Genina and V. V. Tuchin, J. Innov. Opt. Health Sci. **04** [01], 9 (2011).

78) T. Lister, P. A. Wright and P. H. Chappell, J Biomed Opt **17** [9], 90901 (2012).

79) N. Bosschaart, G. J. Edelman, M. C. G. Aalders, T. G. van Leeuwen and D. J. Faber, Lasers Med Sci **29** [2], 453 (2014).

80) Y. Kwon, M. Kim, S. Park, M. Jeong, S. M. Lee, S. H. Lee, W. H. Lee, Y. K. Choi and J. Y. Lee, in *2020 IEEE Symposium on VLSI Circuits* (IEEE, Honolulu, HI, USA, 2020) pp. 1.
81) C. Peng, M. Chen, H. Wang, J. Shen and X. Jiang, IEEE Sensors J. **20** [19], 11221 (2020).
82) C. Peng, M. Chen and X. Jiang, IEEE Sensors J. **21** [6], 7412 (2021).
83) Y. Qin, H. Wang and Y. Liu, SID Symposium Digest of Technical Papers **49** [1], 1604 (2018).
84) D. Tordera, B. Peeters, E. Delvitto, S. Shanmugam, J. Maas, J. Riet, R. Verbeek, R. Laar, T. Bel, G. Haas, L. Ugalde, A. Breemen, I. Katsouras, A. J. Kronemeijer, H. Akkerman, E. Meulenkamp and G. Gelinck, J Soc Inf Display **28** [5], 381 (2020).
85) W.-F. Zhou, L.-Q. Chen, Y.-L. Sun, L. Shi, Z. Liu, F. Guan and D. Wang, SID Symposium Digest of Technical Papers **49** [1], 1014 (2018).
86) Y. Zeng, F. Lu, Q. Yao, H. Yu, Q. Zhang and X. Su, SID Symposium Digest of Technical Papers **52** [S1], 49 (2021).
87) A. K. Jain, Y. Chen and M. Demirkus, IEEE Trans. Pattern Anal. Mach. Intell. **29** [1], 15 (2007).
88) National Institute of Standards and Technology, *American national standard for information systems.* NIST SP 500-245 (National Institute of Standards and Technology, Gaithersburg, MD, 2000) 0 ed.
89) J. M. Libert, S. Orandi and J. D. Grantham, *Comparison of the WSQ and JPEG 2000 image compression algorithms on 500 ppi fingerprint imagery* NIST IR 7781 (National Institute of Standards and Technology, Gaithersburg, MD, 2012) 0 ed.
90) J. J. M. Halls, K. Pichler, R. H. Friend, S. C. Moratti and A. B. Holmes, Appl. Phys. Lett. **68** [22], 3120 (1996).
91) D. E. Markov, J. C. Hummelen, P. W. M. Blom and A. B. Sieval, Phys. Rev. B **72** [4], 045216 (2005).
92) W. A. Luhman and R. J. Holmes, Adv. Funct. Mater. **21** [4], 764 (2011).
93) O. V. Mikhnenko, P. W. M. Blom and T.-Q. Nguyen, Energy Environ. Sci. **8** [7], 1867 (2015).
94) B. A. Gregg, J. Sprague and M. W. Peterson, J. Phys. Chem. B **101** [27], 5362 (1997).
95) H. Najafov, B. Lee, Q. Zhou, L. C. Feldman and V. Podzorov, Nature Mater **9** [11], 938 (2010).
96) A. R. Newmark and U. Stimming, Journal of Electroanalytical Chemistry and Interfacial Electrochemistry **204** [1–2], 197 (1986).
97) A. R. Newmark and U. Stimming, Electrochimica Acta **32** [8], 1217 (1987).

98) S. M. Menke and R. J. Holmes, Energy Environ. Sci. **7** [2], 499 (2014).

99) L. Onsager, The Journal of Chemical Physics **2** [9], 599 (1934).

100) T. Offermans, S. C. J. Meskers and R. A. J. Janssen, The Journal of Chemical Physics **119** [20], 10924 (2003).

101) I. Montanari, A. F. Nogueira, J. Nelson, J. R. Durrant, C. Winder, M. A. Loi, N. S. Sariciftci and C. Brabec, Appl. Phys. Lett. **81** [16], 3001 (2002).

102) A. M. Goodman and A. Rose, Journal of Applied Physics **42** [7], 2823 (1971).

103) A. Liu, S. Zhao, S.-B. Rim, J. Wu, M. Könemann, P. Erk and P. Peumans, Adv. Mater. **20** [5], 1065 (2008).

APPENDIX A

OPTICAL RAY TRACING SIMULATION

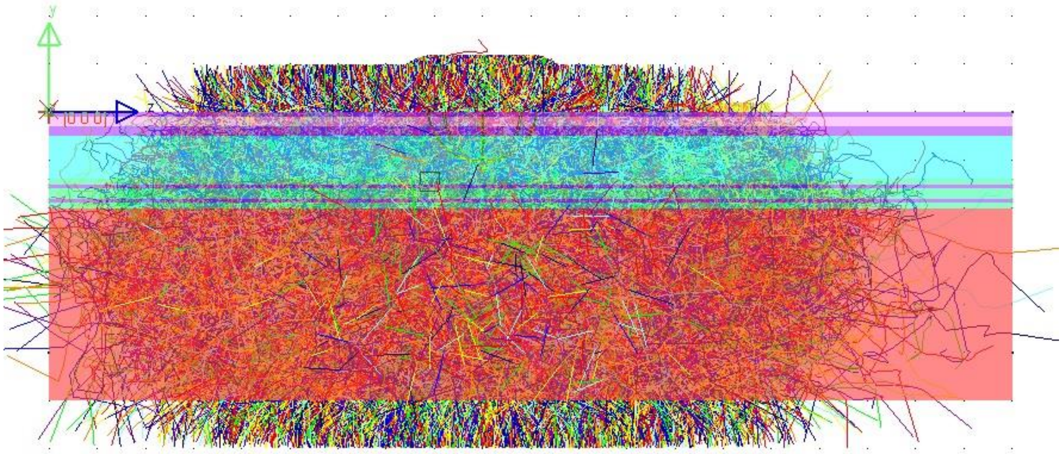

A1: Unfiltered ray tracing for the skin model.

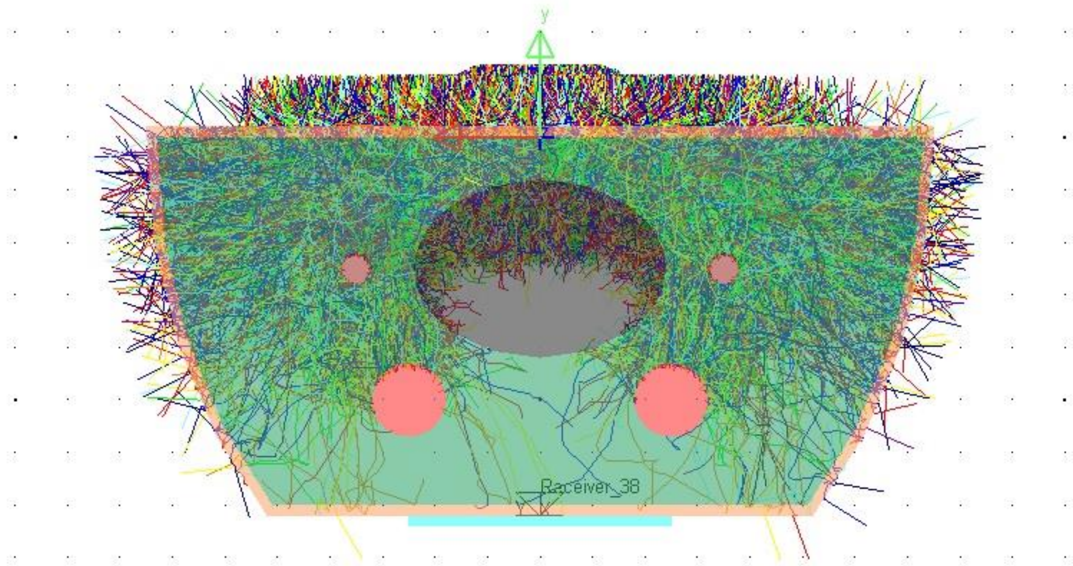

A2: (Front-view) Unfiltered ray tracing for the finger model based on transmission-based system.

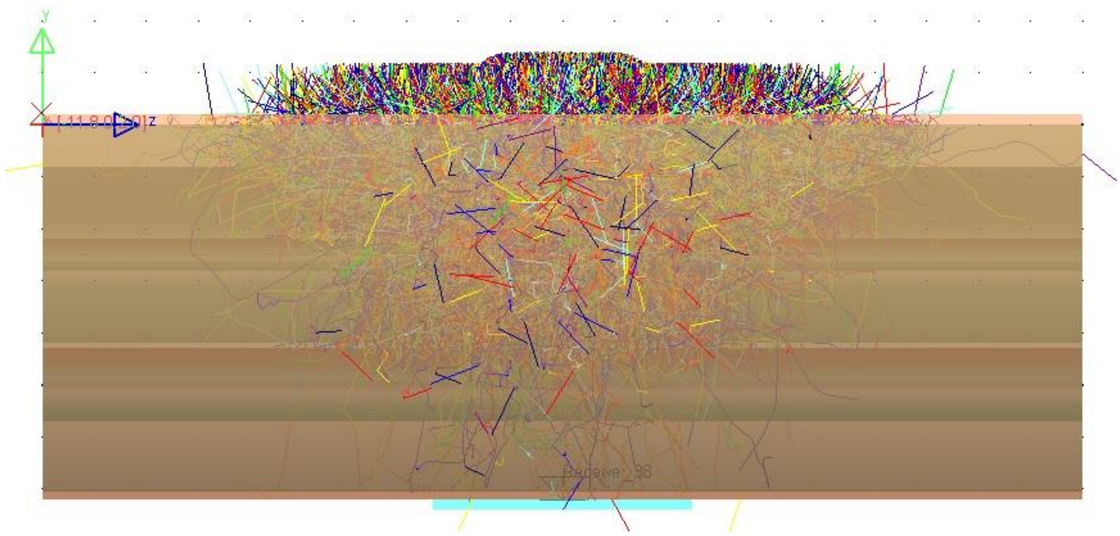

A3: (Side-view) Unfiltered ray tracing for the finger model based on transmission-based system.

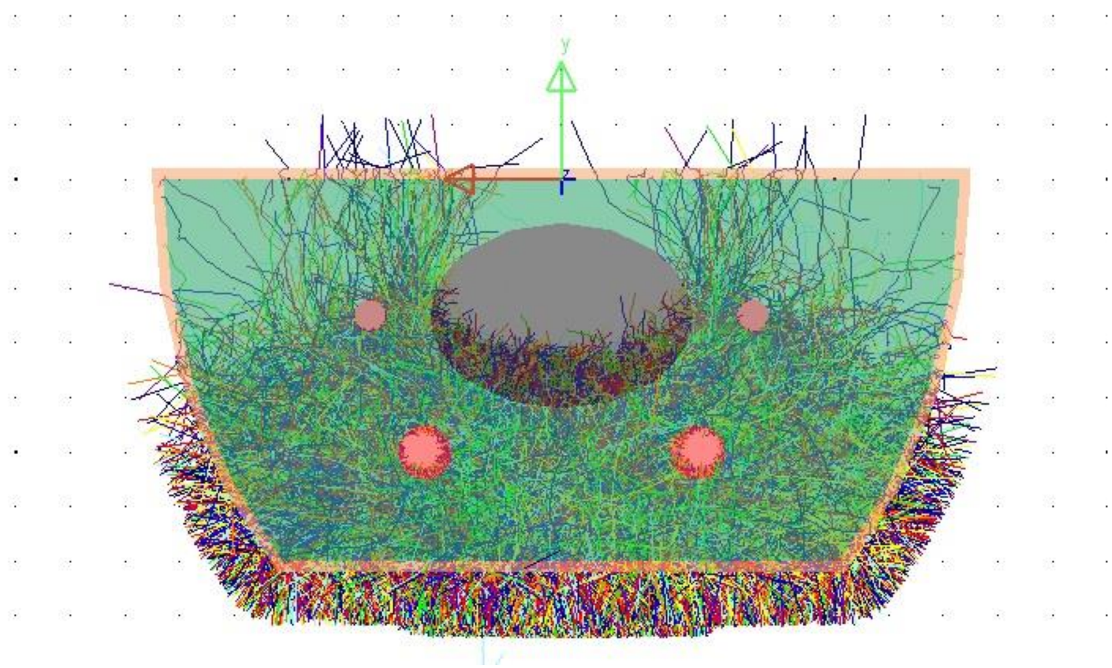

A4: (Front-view) Unfiltered ray tracing for the finger model based on reflection-based system.

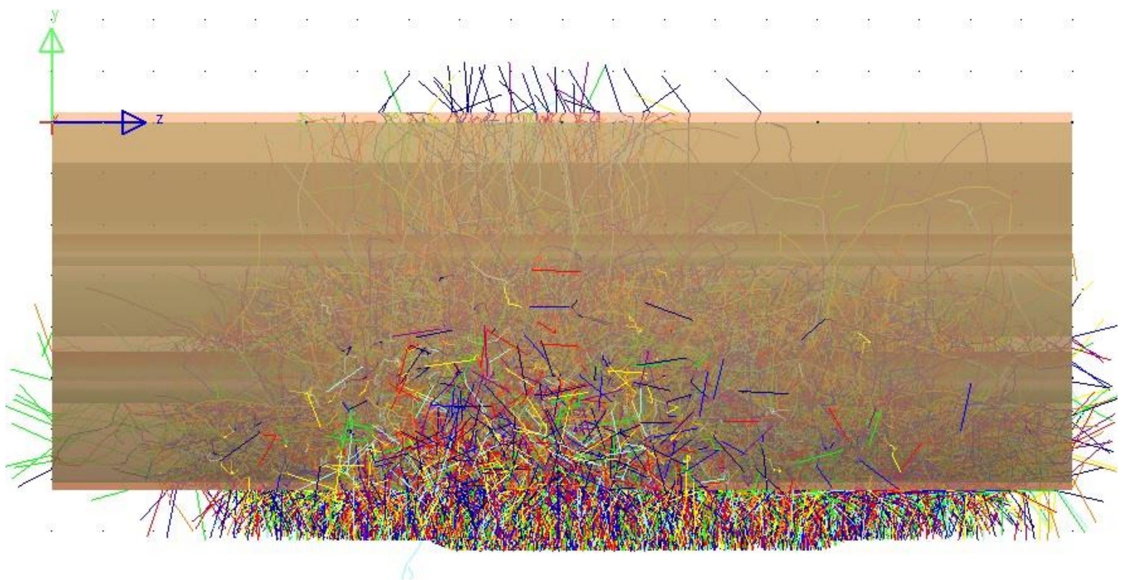

A5: (Side-view) Unfiltered ray tracing for the finger model based on reflection-based system.

APPENDIX B

LAYOUT DESIGN

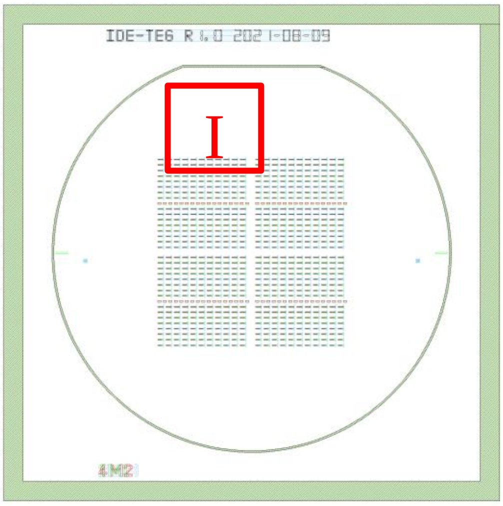

B1: Overview of the photomask for the IDE OPD devices.

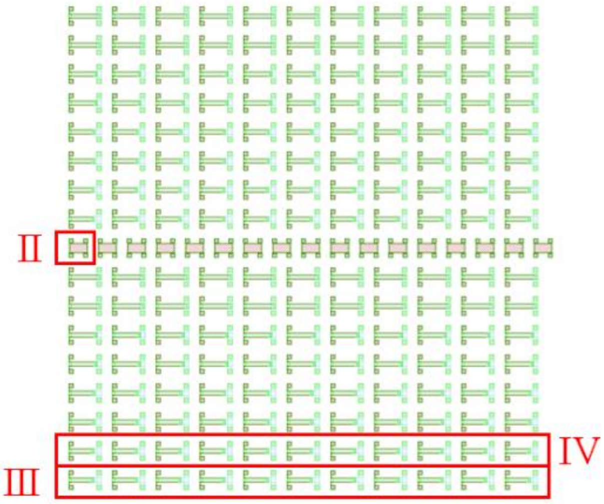

B2: Closed-up view at area I from A1. Area II shows the single OPD device for the verification purpose. Area III shows the IDE OPDs with the most left is the perfectly aligned between the exposed area and opening window. The most right in area III shows the IDE OPDs with 100% shifted to the right side exposing the boundaries of the covered electrodes. Conversely, in area IV the most right is the perfectly aligned device structure and the most left is 100% shifted to the left.

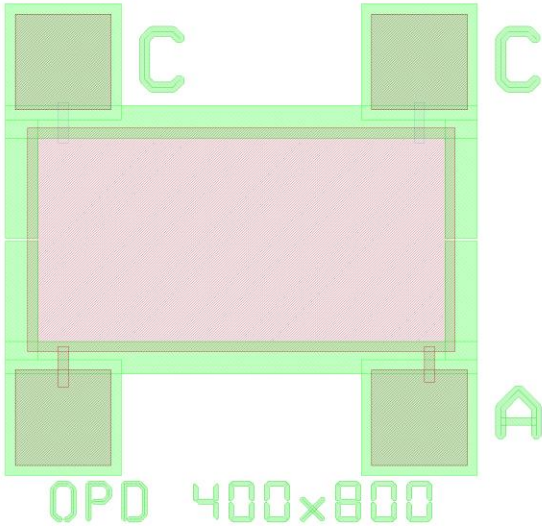

B3: Overview of the single OPD device.

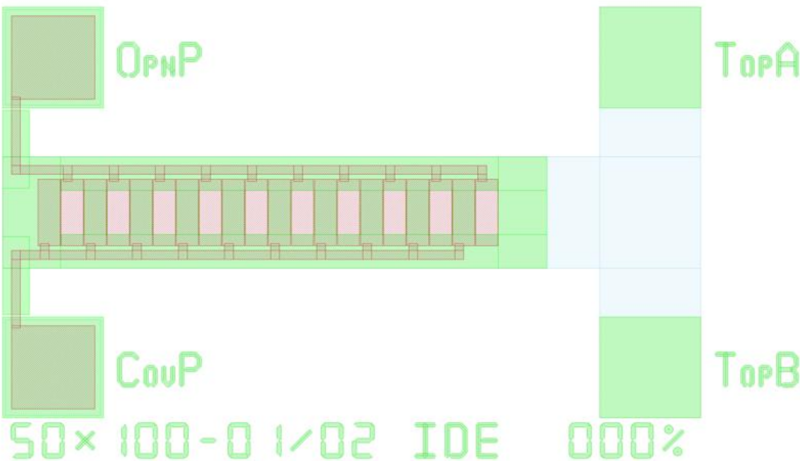

B4: Overview of the IDE OPDs with perfectly aligned between opening window and exposed electrodes for the smallest feature size based on Table 5.1.

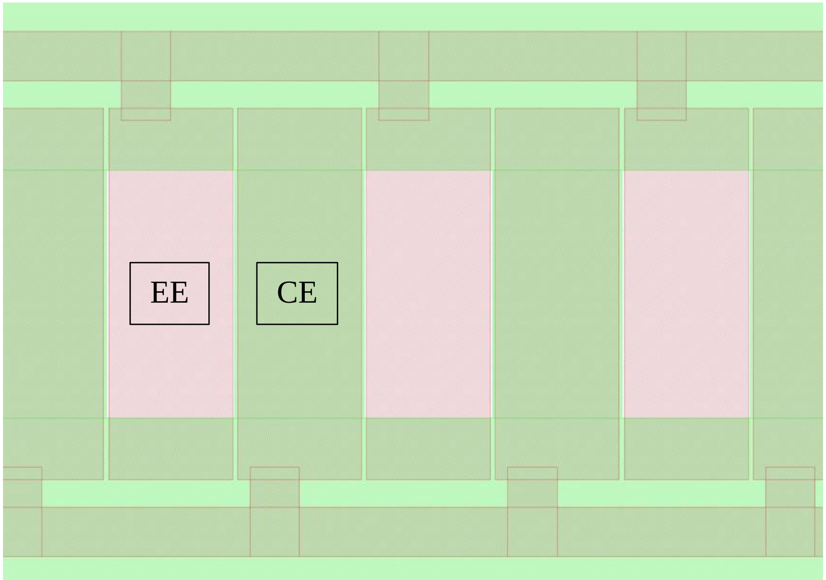

B5: Closed-up view at the exposed electrodes (EE) and covered electrodes (CE).

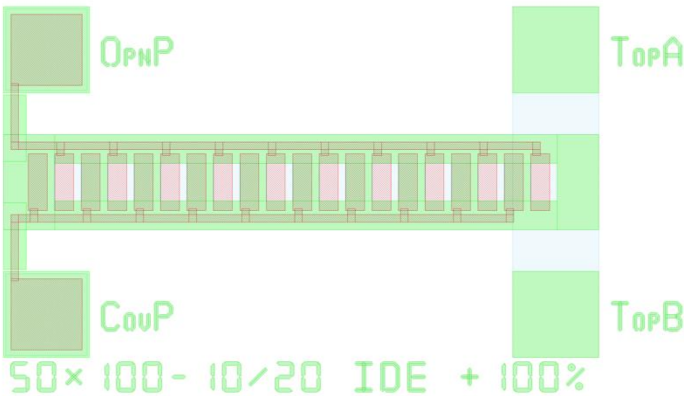

B6: Overview of the IDE OPDs for largest feature size based on Table 5.1 with the opening windows were 100% shifted to the right.

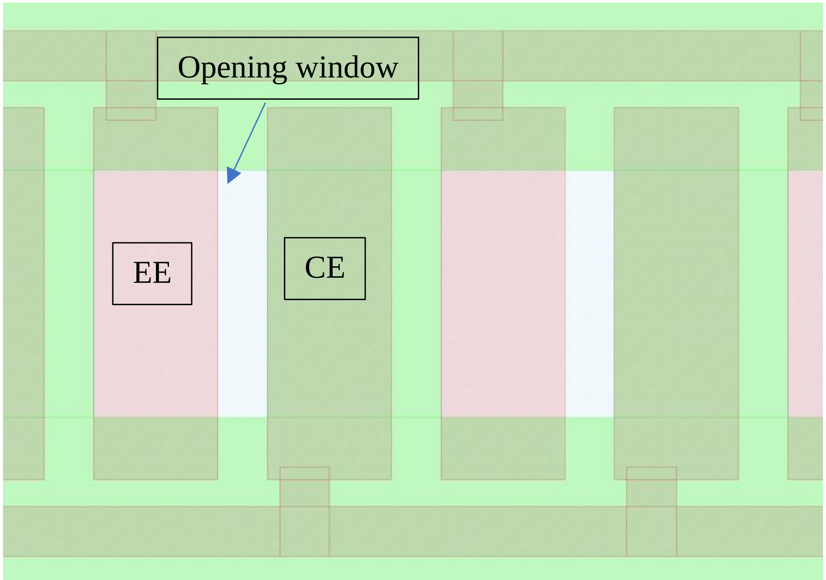

B7: Closed-up view at the electrodes which 100% shifted to the right for the largest feature size used for the device structure.